Trailing Horizontal Vortices in Observed and Numerically Simulated Tornadoes

Maurício I. Oliveira, Ming Xue, and Brett Roberts

ABSTRACT: High-resolution numerical simulations of supercell storms reveal complex distributions of vorticity in the vicinity of tornadoes, especially when visualized in three dimensions. As in the simulations, quasi-horizontal vortices (HVs) are occasionally observed near tornadoes, as condensation tubes wrapping around the tornadoes. In this study, visual observations of a violent tornado and visualizations of a high-resolution simulation based on the same tornado case are combined to document distinct HV structures, which trail the tornado very close to the ground toward its right flank (with respect to the tornado's forward motion), hereafter referred to as "trailing HVs." The analysis shows that trailing HVs are larger and stronger than HVs typically observed around tornadoes. Still, their sense of rotation matches that of other documented HVs, which is consistent with vorticity generation by surface drag and/or baroclinic torques along internal boundaries of relatively warm rear-flank downdrafts. Interestingly, trailing HVs may display smaller spiral vortices circulating their periphery, which can evolve into more complex structures. Visualizations of three-dimensional vorticity show that the trailing HVs are organized through entanglement of large and small HVs along nearby rear-flank internal boundaries. The internal boundaries also serve as focus for along-boundary stretching of vorticity that becomes mostly streamwise at the location of the trailing HV, resulting in HV strengthening. The spiral vortices are associated with the same entangling processes responsible for the parent (larger) trailing HV structure. Moreover, the analysis suggests that trailing HVs may reinforce the surface wind speeds on the right flank of the tornado.

KEYWORDS: Tornadoes; Vortices; Turbulence; Numerical analysis/modeling

AFFILIATIONS: **Oliveira* and Xue**—Center for Analysis and Prediction of Storms, and School of Meteorology, University of Oklahoma, Norman, Oklahoma; **Roberts**—Cooperative Institute for Severe and High-Impact Weather Research and Operations, University of Oklahoma, and NOAA/NWS/NCEP/Storm Prediction Center, and NOAA/OAR/National Severe Storms Laboratory, Norman, Oklahoma
* CURRENT AFFILIATION: Departamento de Física, Universidade Federal de Santa Maria, Santa Maria, Brazil

In recent years, higher-resolution [at $O(10-100)$ m horizontal grid spacing] numerical simulations of supercell storms have presented a variety of substorm-scale structures in greater detail (e.g., Orf et al. 2017). When the grid spacing is on the order of 10 m, simulations of supercells start to resolve complex turbulent structures, some of which are coherent vortex structures. For example, the three-dimensional (3D) visualizations of supercell simulations (Orf et al. 2017; Orf 2019; Oliveira et al. 2019; Yao et al. 2019) show complex vortex–vortex interactions prevalent in the vicinity of rear-flank outflows and near simulated tornadoes. Some of these vortices interact with the main tornado vortex and evolve into quasi-horizontal vortex tubes, which had been referred to as "horizontal vortices" (HVs) in prior studies (Wurman and Kosiba 2013; Knupp et al. 2014; Houser et al. 2016; Bai et al. 2017; Orf et al. 2017; Oliveira et al. 2019).

HVs are occasionally observed on the periphery of real tornadoes as condensation tubes, whenever the pressure drop within their cores is large enough to induce condensation (Knupp et al. 2014; Houser et al. 2016; Bai et al. 2017; Orf et al. 2017; Oliveira et al. 2019). Recent documentation of HVs in tornado footage, close-range mobile Doppler radar observations, and visualizations of tornado-resolving simulations has provided some general insights into their behavior. In visual observations and visualizations of tornado simulations, HVs occur prominently within rear-flank outflows just outside the tornado's outer edge near its right-rear side (looking from behind the tornado) through the left-front low-level sectors (Houser et al. 2016; Bai et al. 2017; Orf et al. 2017; Oliveira et al. 2019). In Doppler radar observations, HVs also appear in the in the vicinity of rear-flank downdraft (RFD) internal boundaries during tornado intensification (Houser et al. 2016). The HV vorticity has a large component to the left of the cold pool outflow winds when the HV is near the surface (i.e., in the crosswise direction of the flow) or in the direction of the flow when the HV wraps around the tornado (when the crosswise horizontal vorticity is exchanged into streamwise vorticity when the flow turns toward the tornado vortex). This suggests that the HVs can be generated by surface friction or by horizontal buoyancy gradient when the air in the internal surge is warmer (for the baroclinically generated vorticity to be of the right sign) (Houser et al. 2016). Since HVs are much weaker than the tornado vortex itself, they seem to behave like passive coherent structures of the flow and are advected by the tornado vortex circulation, evolving into arcs around the tornado. In some situations, HVs are more complex, having downward-bending or spiral structures (Oliveira et al. 2019).

Although HVs have attracted more interest from severe storm researchers as well as storm chasers and severe weather enthusiasts in recent years, several aspects of their nature and importance in supercells remain unknown. For example, are HVs always simply passive features of the flow? Does vorticity contained in the HVs contribute in any significant way to tornado and/or related mesocyclone circulations? Can tornado–HV interactions enhance damaging winds at the surface? Regarding the latter question, the only published report of ground-level damage associated with an HV is that of Bai et al. (2017), who suggested that

a downward-bending HV far downstream of a typhoon-spawned tornado in southern China was responsible for damage to power lines. More studies are needed to better understand the behaviors and dynamics of HVs and whether/how they affect tornadoes and tornadic winds, especially near the surface where damage can occur.

During the 27 April 2011 devastating tornado outbreak in the southeast United States, several strong and violent tornadoes were accompanied by HVs (Knupp et al. 2014). Many of the most intriguing HV–tornado interactions observed on that day occurred during the early stages of the Tuscaloosa–Birmingham, Alabama, EF4 tornado,[1] as it intensified over Tuscaloosa. During this stage of the tornado life cycle, several Tuscaloosa residents video recorded the tornado from multiple locations, affording an opportunity to document some HV structures that have not been discussed much in the literature. More specifically, the visual observations reveal the existence of strong, large HVs that closely trail the tornado around its right flank (with respect to the tornado's forward motion) very near the ground, producing strong wind fields. This feature also tends to retain its structure and position relative to the tornado before wrapping around the tornado whereas smaller HVs tend to wrap around tornadoes without a trailing tail (Orf et al. 2017; Oliveira et al. 2019). In light of these characteristics, we refer to these large HVs as "trailing HVs." In addition, some videos show that these trailing HVs can interact with smaller HVs to create complex 3D vortical structures in the vicinity of the tornado, rendering these features even more interesting.

The purpose of this article is to document and provide some preliminary understanding of the trailing HV structures identified in selected videos of the Tuscaloosa tornado. To gain insight on the 3D structure and evolution of trailing HVs beyond the limited clues available in the video recordings, we present visualizations and a brief qualitative analysis of a high-resolution idealized numerical simulation of the Tuscaloosa tornado case, which contains vortical features with similar characteristics of the visually observed trailing HVs. It is hoped that this study will highlight the potential importance of HVs and their interactions with tornadoes, as well as encourage more investigations on coherent vortical structures in supercell outflows and how they may affect tornado evolution.

[1] Hereafter simply referred to as the "Tuscaloosa tornado."

Model setup and base-state environment

The 3D, nonhydrostatic Advanced Regional Prediction System (ARPS; Xue et al. 2000, 2001, 2003) is used for the numerical experiment. The ARPS was designed with the purpose of simulating convective-scale phenomena and has been used extensively in studies on the dynamics, simulation, and prediction of tornadoes (Snook and Xue 2008; Noda and Niino 2010; Schenkman et al. 2014; Xue et al. 2014; Dawson et al. 2015; Roberts et al. 2016; Roberts and Xue 2017; Oliveira et al. 2019; Snook et al. 2019; Roberts et al. 2020). To resolve fine-scale HV structures at low levels, a horizontal grid spacing of 30 m is used along with a vertical grid spacing that stretches from 2 m at the surface to 200 m above 10 km above ground level (AGL). This setup yields three levels of scalar variables (as well as horizontal wind components) below 20 m AGL (1, 6, and 16 m AGL) and an average vertical grid spacing of 30.8 m below 650 m AGL. Given the grid configuration, both the large and small time steps used by mode-splitting time integration (Klemp and Wilhelmson 1978; Xue et al. 2000) are set to 0.05 s to ensure time integration stability in the presence of tornadic wind speeds.[2] A summary of the model setup and parameters is provided in Table 1. The experiment is integrated forward in time for 3 h to encompass the entire life cycle of a simulated tornado.

Model output is saved every 60 s during the nontornadic phase of the storm (0–6,600 s) and every 2 s for the remainder

[2] Because vertical acoustic waves are integrated using an implicit scheme in the ARPS, the small time step is limited by horizontal grid spacing only. The large time-step size is limited by both horizontal and vertical Courant numbers. Given that the vertical grid spacing is much smaller at the low levels, the usable large time step is comparable to the small time step.

Table 1. ARPS configuration.

Parameter	Description
Grid points	3,003 × 3,003 × 93 (838.7 million)
Domain extent	90 km × 90 km × 18.2 km
Horizontal grid spacing	$\Delta x = \Delta y = 30$ m
Vertical grid spacing	$\Delta z_{min} = 2$ m, stretched to 200 m above 10 km AGL
Rayleigh damping layer	Applied above 14 km AGL
Advection scheme	Fourth order in both horizontal and vertical directions
Microphysics	Mansell et al. (2010) double moment
Turbulence closure	1.5-order TKE based on Moeng and Wyngaard (1988)
Numerical diffusion	Fourth order in both horizontal and vertical directions (cfcm4h = 10×10^{-3} m^4 s^{-1}; cfcm4v = 2×10^{-3} m^4 s^{-1})
Lateral boundary conditions	Open radiative
Lower boundary condition	Semislip, with $C_d = 0.028$ (roughness length = 9.16 cm)
History output frequency	60 s between 0 and 6,600 s; 2 s afterward until 10,800 s

of the simulation, including the pretornadic phase of the storm (6,600–6,998 s) and the full life cycle of the tornado (7,800–10,800 s). Given that this study focuses on analyzing vortex structures around the tornado and surrounding storm-scale features, data are saved only in an 18 km × 18 km × 18.2 km box centered on the low-level (0–3-km) mesocyclone to save disk space.

The base-state environment of the tornadic supercell simulation is shown in Fig. 1. The thermodynamic profile is similar to that used by Oliveira et al. (2019) and is extracted from a 3-km Weather Research and Forecasting Model ensemble analysis valid at 2100 UTC 27 April 2011 at a grid point off the right flank of a supercell corresponding to the Tuscaloosa storm (Yussouf et al. 2015). The environment features a combination of high conditional instability and very strong low-level shear [e.g., 3,424 J kg^{-1} mean-layer convective available potential energy (MLCAPE) and 486 m^2 s^{-2} 0–1-km storm-relative helicity (SRH); see the convective parameters at the bottom-right part of Fig. 1], a setup known to be conducive to violent tornadoes (Rasmussen 2003; Coffer et al. 2019; Taszarek et al. 2020). The conditions are also consistent with observations and mesoscale model outputs for 27 April 2011 around the time of the Tuscaloosa tornado (Knupp et al. 2014). In our earlier test simulations, convective initiation was achieved in this environment by releasing a 3–4-K warm bubble within the model domain. However, due to the negligible mean-layer convective inhibition (MLCIN ~0 J kg^{-1}), numerous undesired convective cells formed elsewhere in the domain, contaminating the main supercell storm and its environment.

To circumvent this issue, a temperature increment of 1.8 K is added just below 1.5 km AGL, which smoothly decreases upward and downward according to a fourth-degree polynomial function (Oliveira et al. 2019). This slightly increases static stability in the upper boundary layer and increases the magnitude of MLCIN to 19 J kg^{-1}. With this procedure, a warmer (6 K) bubble is needed to overcome the augmented MLCIN. In addition, the winds in Fig. 1 are ~20% stronger relative to those used in Oliveira et al. (2019) below 2 km AGL. This modification enables the simulation of more intense tornadoes compared to the experiments of Oliveira et al. (2019). Other differences in the model configuration used in the current simulation and that of Oliveira et al. (2019) may also influence the production of stronger tornadoes. These differences include the use of an updated version of the ARPS model, a larger domain, smaller grid spacing, and double-moment microphysics in the current simulation. In general, the stronger, longer-lived simulated tornado in this study is more consistent with the observed Tuscaloosa tornado.
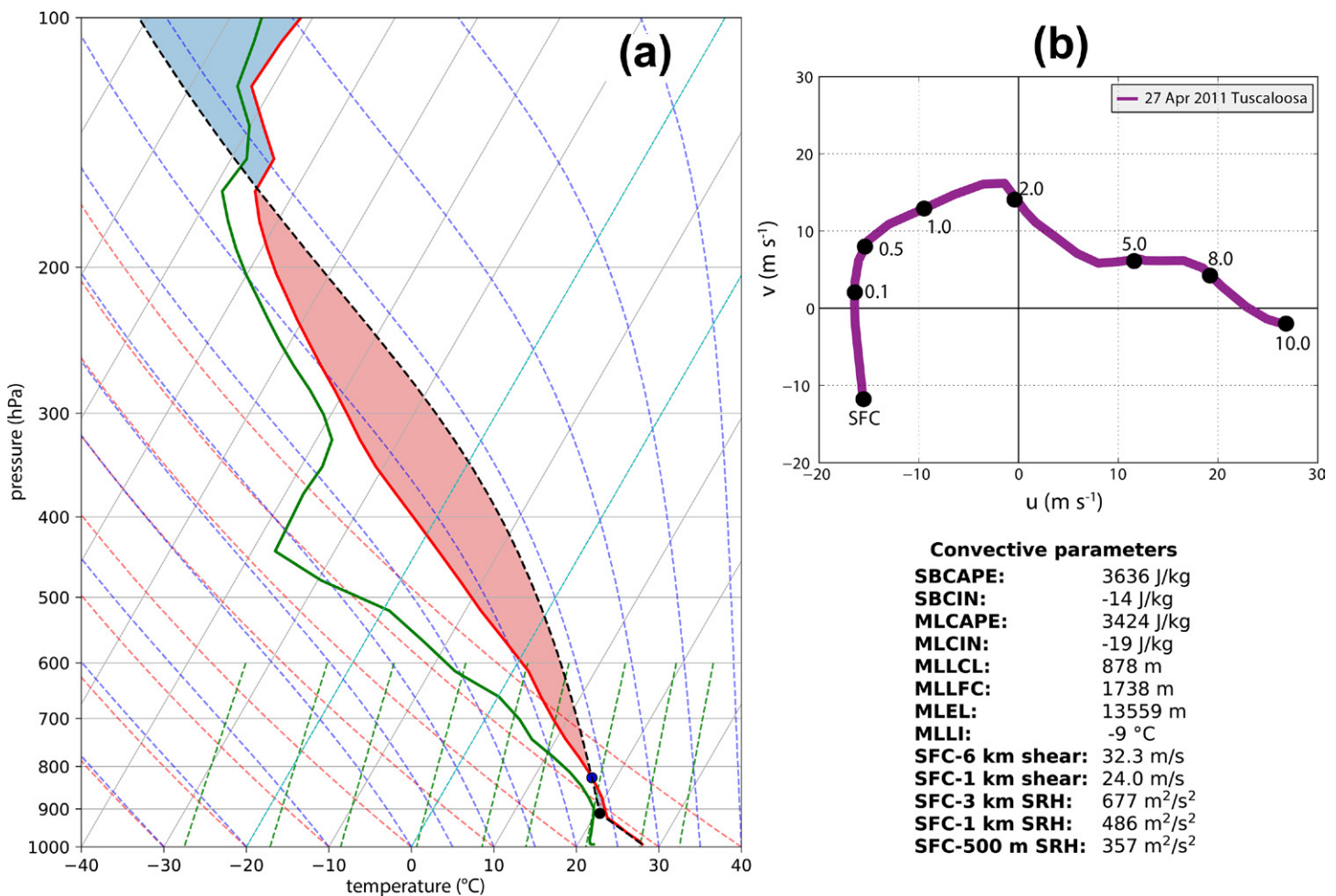
Fig. 1. (a) Skew *T*–log*p* diagram for the idealized tornadic supercell experiment. The red (green) solid line represents environmental temperature (dewpoint) in °C. The black dashed line denotes the temperature for an ascending surface-based parcel. Areas of positive (negative) buoyancy are highlighted by semitransparent red (blue) shading. The black and blue dots represent the lifting condensation level and level of free convection, respectively. (b) Hodograph for storm-relative winds between the surface and 10 km AGL. A ground-motion vector (u = 11 m s^{-1}, v = 17 m s^{-1}) was subtracted from the wind profile to induce the storm to remain quasi stationary near the center of the domain. Black dots are heights (in km AGL). Some relevant convective parameters are shown in the bottom-right sector of the figure.

Recent studies have pointed to the importance of surface drag in the generation of tornadoes and possibly also HVs in numerical simulations (Schenkman et al. 2014; Markowski 2016; Roberts et al. 2016; Yokota et al. 2018; Oliveira et al. 2019; Roberts et al. 2020; Tao and Tamura 2020; Fischer and Dahl 2022). Our experiment parameterizes the effect of surface drag via a semislip lower boundary condition, where the negative momentum flux at the surface is parameterized based on the Monin–Obukhov similarity theory (Markowski et al. 2019), using the wind speed at the first model level above ground (1 m AGL in our case) and a drag coefficient (C_d) of 0.028. This C_d corresponds to a roughness length value between those of the C_d = 0.005 and C_d = 0.01 experiments in Roberts et al. (2020), where the first model level is at 10 m AGL. In idealized storm simulations, when the frictional force is not in balance with the horizontal pressure gradient force and the Coriolis force, surface drag tends to slow the low-level environmental wind, altering the specified environmental flow condition the simulated storm is embedded in. To avoid this complication, we employ the "geotriptic wind balance" (hereafter GWB) technique developed in Dawson et al. (2019). In brief, this method calculates a pseudo–pressure gradient force (PPGF) as the residual between the frictional force and Coriolis force at the beginning of model integration and applies it to the momentum equations every time step. This ensures a three-way geotriptic balance in the storm environment

away from storm-induced perturbations, and the PPGF acts as an approximation of the real pressure gradient force in nature. Therefore, the storm environment as defined by the initial sounding remains unaltered by the presence of surface drag. A detailed description of the GWB method and related testing are found in Dawson et al. (2019).

A recent paper by Davies-Jones (2021) suggests that the methodology used by Dawson et al. (2019), Oliveira et al. (2019), and Roberts et al. (2020) to maintain a steady-state environment in the presence of surface friction in idealized storm studies may introduce an artificial source of vorticity into the simulation so as to alter the storm dynamics. However, the purpose of the PPGF introduced in the GWB procedure is to approximate a real, large-scale pressure gradient force, which maintains a three-force balance with the Coriolis and frictional forces so that the environmental shear does not change in the presence of surface friction. Although the PPGF term is often large in the first model layer above ground (and generally in this layer only), this is only true because the PPGF is prescribed in part to offset the frictional force acting on the environmental wind, which is itself large near the lower boundary for physically valid reasons. In this way, the PPGF mirrors the vertical profile of a real pressure gradient force over rough surfaces in nature. Furthermore, the sum of the PPGF and drag acting on the base-state wind always equals the negative of Coriolis, a term with small-enough magnitude that it is often neglected via scale analysis when analyzing supercells and tornadoes. Thus, the degree to which the PPGF generates unphysical vorticity is likely overstated by Davies-Jones (2021), and that study's moniker of "invented force" for our PPGF ignores the fact that it mirrors a real large-scale pressure gradient force to some reasonable approximation (with storm-scale pressure perturbations in the simulation inducing additional pressure gradient forces which are explicitly modeled). As such, results from simulations such as ours herein that use the GWB procedure should be at least qualitatively useful, rather than being dominated by the effects of a spurious force with no analog in real storm environments. Further quantitative analyses will be needed to prove otherwise.

In this study, 3D visualizations are employed to assess the structure and evolution of HVs and the attendant tornado. The visualizations are performed using the volume rendering feature of the Visualization and Analysis Platform for Ocean, Atmosphere, and Solar Researchers (VAPOR; Li et al. 2019) software.

Overview of the simulated supercell and tornado

Before presenting an analysis of trailing HVs, we first provide a general assessment of the simulated storm and the tornado it spawns. The overall evolution of the storm is depicted in Fig. 2 in terms of time–height cross sections of maximum vertical velocity (w_{max}), minimum perturbation pressure (p'_{min}), and maximum vertical vorticity (ζ_{max}) in the lowest 5 km of the 18 km × 18 km subdomain. The initial updraft impulse develops into deep convection by 1,800 s and splits into left-moving and right-moving cells by 2,400 s (not shown). The right-moving cell, which is the storm of interest in this study, moves to the northwest, while the left-moving cell moves to the north and eventually exits the simulation domain (not shown). By 3,600 s, the right-moving storm is fully developed into a supercell, with a relatively steady midlevel updraft containing $\zeta_{max} > 0.01$ s^{-1} above 1 km AGL. The storm moves northwestward between 3,600 and 7,200 s, eventually slowing so that the storm's updraft becomes nearly centered in the domain. At 7,200 s, the storm displays characteristic supercell structures at low levels (Lemon and Doswell 1979), including a well-defined forward-flank precipitation core, a developing hook echo, and a rear-flank gust front (RFGF) (Fig. 3a). During the 3,600–7,200-s period, the supercell cycles a few times, as indicated by transient pulses in w_{max} and ζ_{max} in Figs. 2a and 2c, respectively. However, no tornado-like vortex develops in the first 2 h of model integration.
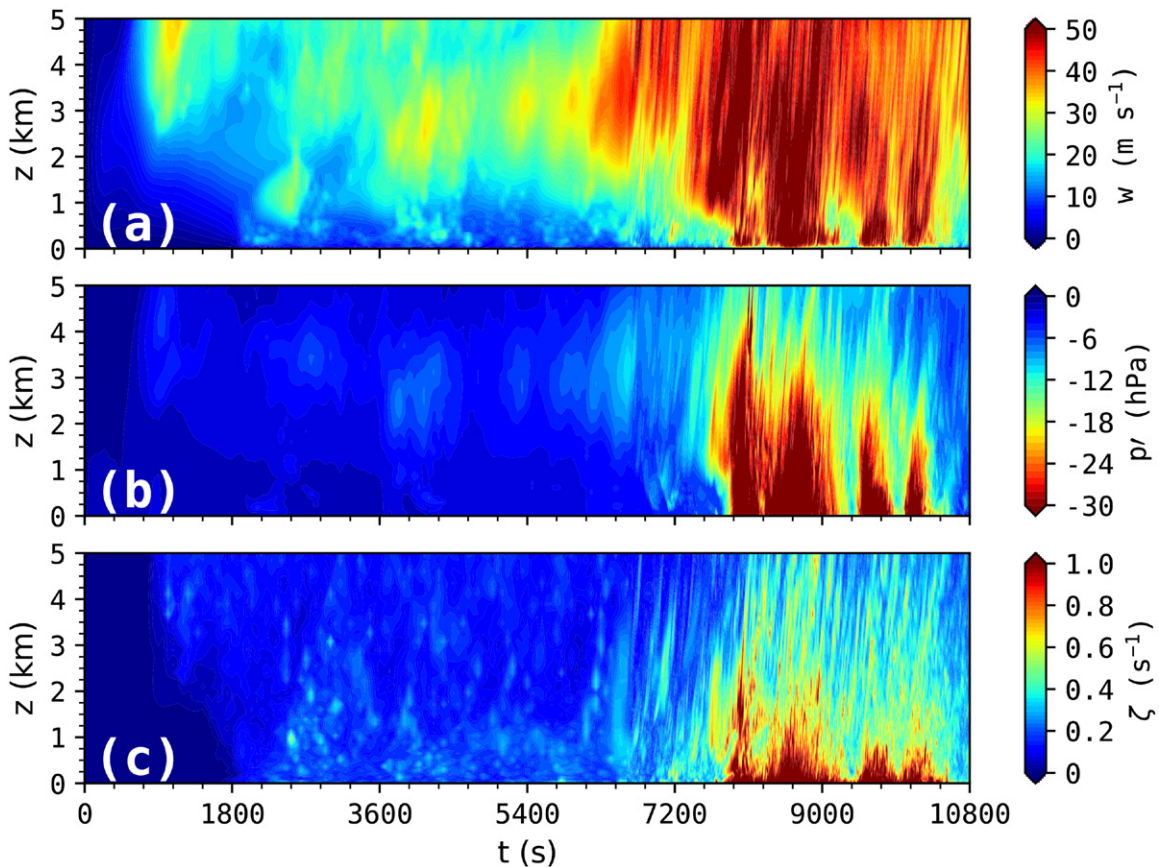
Fig. 2. Time–height cross section of 0–5-km (a) maximum updraft, (b) minimum perturbation pressure, and (c) maximum vertical vorticity in the subdomain, valid from 0 to 10,800 s.

Dramatic changes in the storm's behavior commence around 7,200 s and precede tornadogenesis. A strong updraft and a pressure deficit develop simultaneously in the 1–3 km AGL layer and build downward toward the surface in the ensuing minutes (Figs. 2a,b). As this trend continues, small, short-lived pockets of high ζ_{max} begin to form and intensify rapidly near the surface, indicating that the strengthening low-level updraft is enhancing stretching of low-level vertical vorticity (Fig. 2c). This behavior has been extensively described in previous numerical simulations of tornadic supercells and is attributed to the generation of strong dynamic vertical perturbation pressure gradient acceleration (DVPPGA) within low-level mesocyclones during the pretornadic phase (Rotunno and Klemp 1985; Grasso and Cotton 1995; Wicker and Wilhelmson 1995; Noda and Niino 2010; Markowski and Richardson 2014; Coffer and Parker 2017; Coffer et al. 2017; Orf et al. 2017; Roberts and Xue 2017; Coffer and Parker 2018; Yokota et al. 2018; Flournoy et al. 2020). These studies attribute the generation of low-level DVPPGA to rotationally induced pressure deficits resulting from tilting and stretching of large low-level streamwise horizontal vorticity available in the storm environment (Rotunno and Klemp 1985; Davies-Jones et al. 2001; Markowski and Richardson 2014; Coffer and Parker 2017; Coffer et al. 2017; Coffer and Parker 2018; Goldacker and Parker 2021), later augmented by baroclinic (Klemp and Rotunno 1983; Rotunno and Klemp 1985; Wicker and Wilhelmson 1995; Orf et al. 2017) or frictional (Roberts and Xue 2017) processes within the parent supercell. Further intensification of the low-level updraft eventually culminates in tornadogenesis[3] by 7,800 s (Fig. 3b), illustrated in Figs. 2b and 2c as an explosive development of a high-ζ_{max}, low-p'_{min} column extending up to 5 km AGL.

Shortly after formation, the tornado intensifies rather rapidly, attaining instantaneous ground-relative wind speeds of 100 m s^{-1}

[3] A "tornado" is defined herein as a deep ($z > 1$ km), strong ($\zeta_{max} > 0.3$ s^{-1}, $p'_{min} < -10$ hPa) coherent vortex with wind speeds exceeding the minimum criteria for EF0 strength at 10 m AGL, the level at which wind speeds are assessed for EF-scale rating (Edwards et al. 2013).
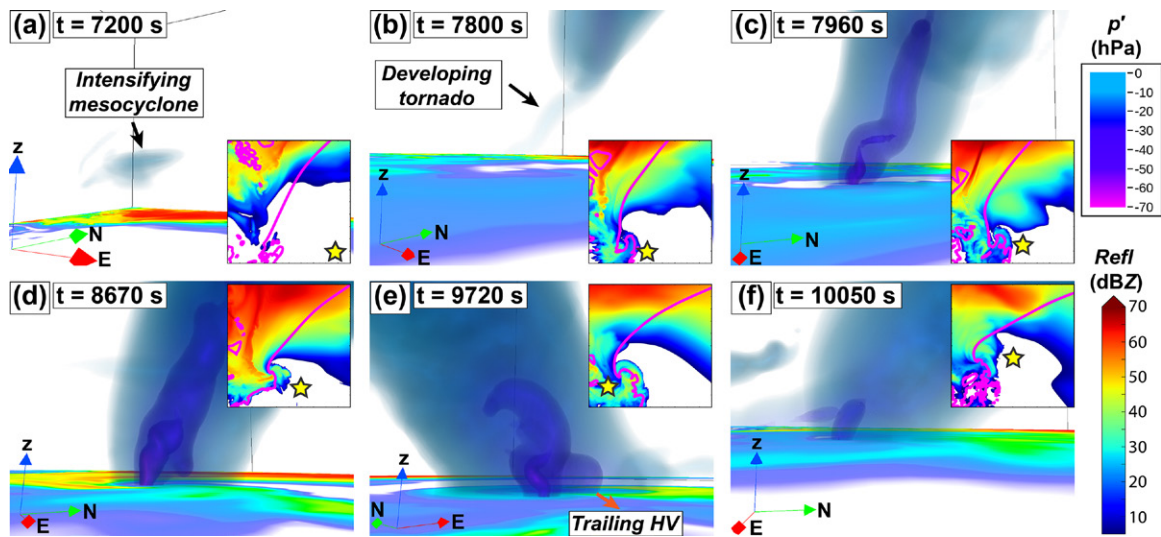
Fig. 3. Evolution of the simulated supercell and its attendant tornado in the volume-rendered perturbation pressure (p') field at (a) 7,200, (b) 7,800, (c) 7,960, (d) 8,670, (e) 9,720, and (f) 10,050 s. The p' field is rendered where $p' < -5$ hPa in (a) and $p' < -7.5$ hPa in (b)–(f). Reflectivity is shaded in dBZ at the lowest grid level (1 m AGL) in the 3D plots and in the top view shown in the insets at the corners of each panel. The −1-K density potential temperature perturbation is denoted by the magenta contour in the insets. The camera's location relative to the storm/tornado is represented by the yellow star. The green, red, and blue arrows point to the north, east, and up, respectively.

(above the EF5 threshold) by 7,960 s (Fig. 4) and a helical structure (Fiedler 2009; Dahl 2021), as visualized using the perturbation pressure field (Fig. 3c). After its initial intensification, the strength and structure of the tornado fluctuates considerably throughout the remainder of its life span (Fig. 4), reaching EF5 intensity (10-m wind speed > 90 m s^{-1}) several times during the period. During its third intensification stage, the tornado, located 1–1.5 km to the west of the RFGF (Fig. 3d), attains its highest intensity around 8,670 s, with ground-relative surface winds in excess of 120 m s^{-1}, p'_{min} lower than −110 hPa and ζ_{max} of nearly 4 s^{-1}. Following its peak stage, hook-echo precipitation fully encircles the tornado leading to a gradual weakening trend in the subsequent 600 s (Fig. 4). Though embedded in rain, a fourth intensification phase begins at 9,300 s, when the tornado again reaches EF5 strength (Fig. 3e). It is during this stage, specifically from 9,500 to 9,800 s, that a structure similar to a trailing HV develops (seen as a large curling horizontal low-p'_{min} lobe southeast of the tornado in Fig. 3e). Finally, the tornado intensifies one last time by 10,050 s (Fig. 3f) before finally dissipating by 10,500 s in the storm's precipitating core. The total duration of the tornado is ~45 min.

Visual characteristics of trailing HVs

There were numerous social media (YouTube) posts of videos capturing the Tuscaloosa tornado as it formed and tracked through the city. Three videos of the early stages of the Tuscaloosa tornado highlighting the trailing HVs are used in our analysis. These videos were taken by Ryne Chandler and Nate Hughett (hereafter referred to as "Chandler/Hughett video"), Jason Rosolowski ("Rosolowski video"), and Tom Deelo ("Deelo video"), who generously granted permission for use in this study. Two of the videos, the Chandler/Hughett and Rosolowski videos, were also used and geolocated by Karstens et al. (2013) in their assessment of tree fall damage patterns induced by the Tuscaloosa tornado. We conducted an independent geolocation procedure using Google Maps (maps.google.com) spatial matches to video frames using the three videos to ascertain the precise location where the videos were taken. Both Chandler/Hughett and Rosolowski video locations matched accurately those shown in Karstens et al. (2013); in addition, the Deelo video location was determined successfully using the location information available in the video's description. The geolocated video
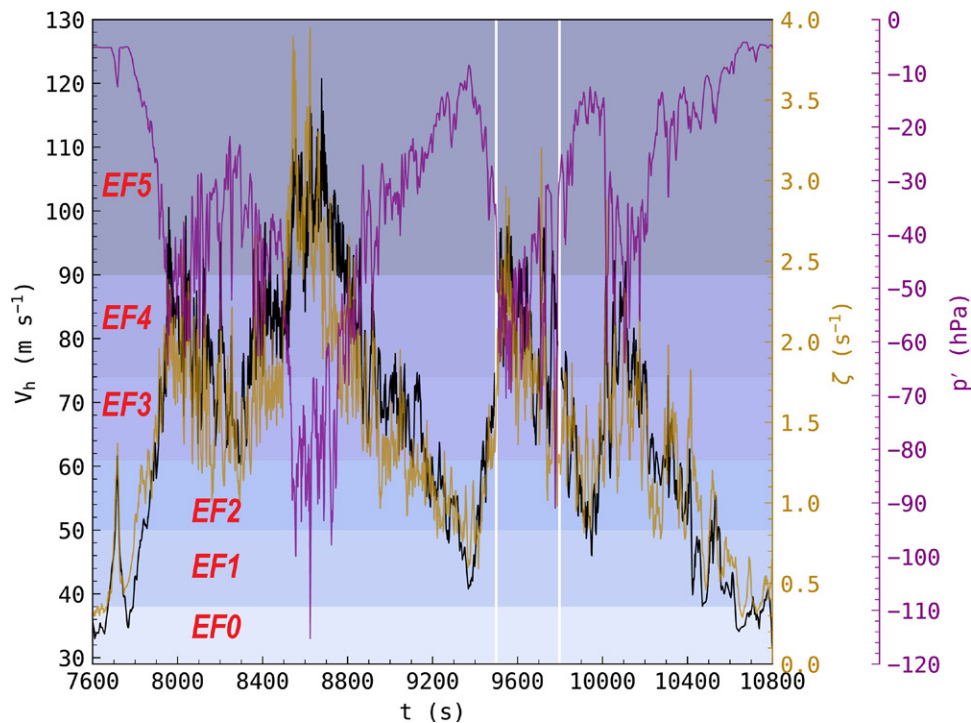
Fig. 4. Time series of maximum ground-relative horizontal wind speed (m s^{-1}; black), minimum perturbation pressure (hPa; purple), and maximum vertical vorticity (s^{-1}; golden) at 10 m AGL in the subdomain, valid from 7,600 to 10,800 s. The semitransparent horizontal bars in the background denote EF-scale wind speed ranges. The vertical white lines are plotted at 9,500 and 9,800 s, respectively, to demark the formation and decay of the simulated trailing HV in Fig. 9.

sites relative to the tornado's early damage path are shown in Fig. 5, which is adapted from Fig. 13 of Karstens et al. (2013). The video's names, observer's locations, their distances to the tornado's center line (determined from Fig. 5) as well as the hyperlinks to the videos URLs are shown in Table 2.

The trailing HVs occurred during two instances of the early life cycle of the Tuscaloosa tornado. The first instance was filmed at close range (Table 1) in both Deelo's and Chandler/Hughett's videos, from which selected frames are shown in Figs. 6 and 7, respectively. In both figures, the camera initially points to the northwest and gradually shifts to the north-northeast to follow the northeastward-moving tornado. The main aspects of trailing HVs can be gained by a combined analysis of Figs. 6 and 7. In Figs. 6a and 6b, despite the contamination by backlighting, the trailing HV can be discerned in the foreground, as a large, near-surface quasi-horizontal tube tangent to the outer edge of the tornado's condensation funnel and present in all panels. The trailing HV is oriented from the rear (southwest) toward the forward flank (northeast) of the tornado, with its forward sector wrapping around the tornado. These observations are better illustrated by the wider perspective shown in Fig. 7, despite the poor contrast between the tornado and the trailing HV in Figs. 7a and 7b. The rotation of the trailing HV is characterized by extremely intense helical flow into the forward flank of the tornado, as denoted by the hypothetical streamlines in Figs. 6b and 7b.

The longevity of the trailing HV relative to smaller HVs can also be seen in Figs. 6 and 7. Smaller-scale HVs are seen moving rapidly around the tornado in Figs. 6b, 6c, 7a, and 7b (indicated by blue arrows). Conversely, the trailing HV approximately preserves its size, intensity, and position relative to the tornado throughout the entire period shown in Figs. 6 and 7a–g (visible for 12 and 13 s, respectively). This indicates that, unlike smaller-scale HVs, trailing HVs may be associated with larger, more persistent storm-scale structures, such as RFD internal boundaries in the right-rear sector of the tornado. It is interesting to notice, though, that

Table 2. Information on the Tuscaloosa tornado videos used in the study.

Videographer(s)	Location (lat, lon)	Approx. distance to tornado (m)	Video's online address
R. Chandler/N. Hughett	33.179 79°N, 87.556 92°W	500–600	www.youtube.com/watch?v=TIx26tN6pCk
T. Deelo	33.175 89°N, 87.554 21°W	1,000	www.youtube.com/watch?v=I8FceUTsJ84
J. Rosolowski	33.194 72°N, 87.524 20°W	150–200	www.youtube.com/watch?v=5ohIVzlZLuQ

the downstream portion of the trailing HV eventually tilts upward into the forward flank of the tornado (Figs. 6d–h and 7d–h).

In Fig. 8, the tornado has just passed to the north of the observer, who watched the tornado moving due northeast and is located immediately to the southeast of the tornado. The trailing HV is seen as a horizontal condensation funnel attached to right-forward edge of the tornado, with its tail closer to the observer (Fig. 8a). From this perspective, not only is the strong helical flow of the trailing HV more evident, but also the upward motion at the interface between the vortex and the tornado just above the ground. In fact, the strong upward jet in this region can be seen violently lifting off buildings materials in Figs. 8b and 8c (yellow arrows). Therefore, the still images and the video suggest that the HV may also create damaging surface winds in the periphery of the tornado.

The visual aspects of the trailing HV collectively provide clues regarding their formation mechanisms. The sense of rotation of trailing HVs (or their vertical motion pattern) and their position relative to the tornado are consistent with radar-detected and numerically simulated HVs observed to the south and east of intensifying tornadoes and near RFD internal boundaries,
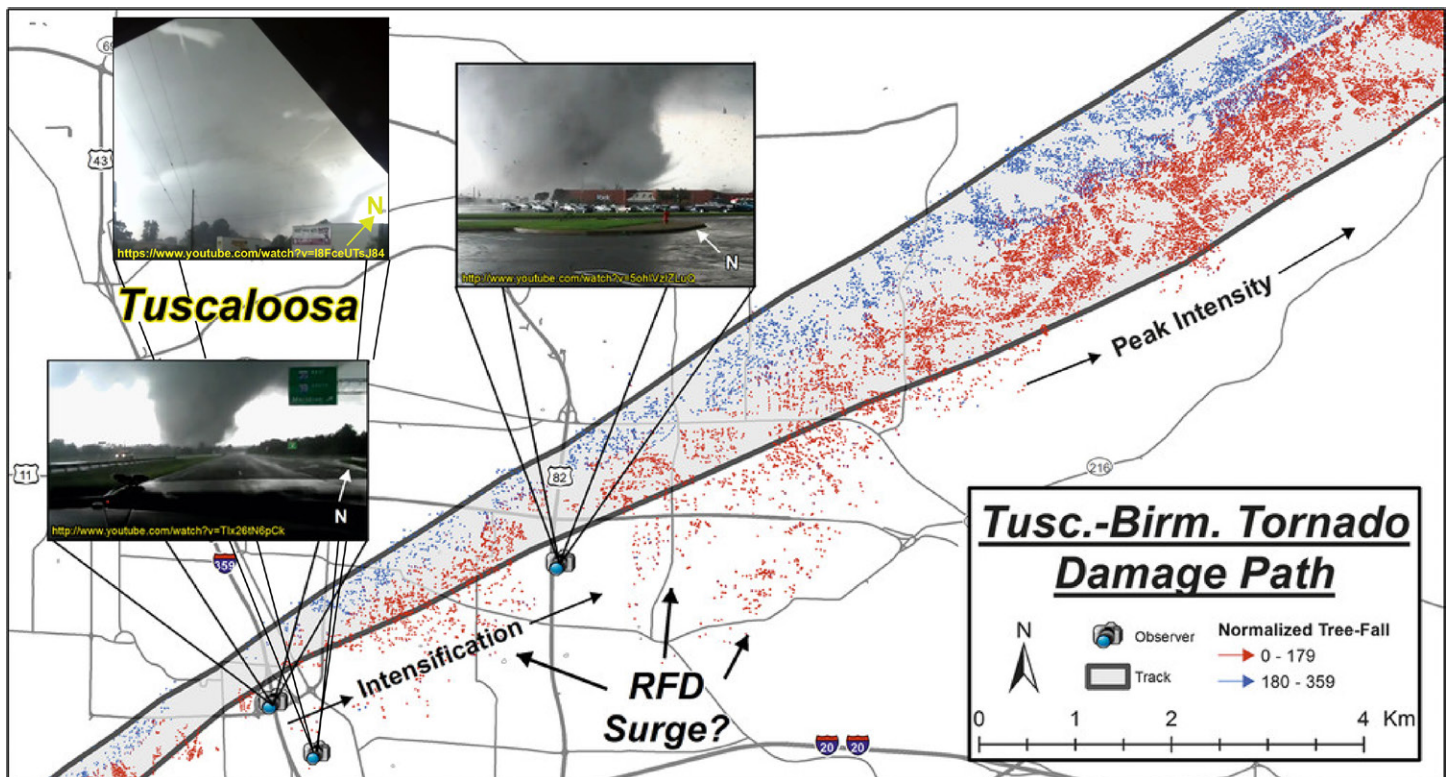
Fig. 5. Early segment of the Tuscaloosa tornado damage path highlighting tree-fall damage (represented by small blue and red arrows). The figure is adapted from Fig. 13 of Karstens et al. (2013) to include the location of the video shown in Fig. 6 of this study. The camera icons are the location where the videos were taken. Image provided through the courtesy of Dr. Christopher Karstens.

as shown by Houser et al. (2016) and Oliveira et al. (2019). These studies suggest that the vorticity in HVs is produced via frictional torques within RFD internal surges and possibly also by baroclinity at the leading edge of positively buoyant RFD surges (Skinner et al. 2011; Marquis et al. 2012; Schenkman et al. 2016). The frictional mechanism is generally more effective in generating horizontal vorticity near the ground (Schenkman et al. 2014; Roberts et al. 2016, 2020; Tao and Tamura 2020). The sign of the horizontal vorticity generated by these mechanisms matches the sense of rotation observed in the HVs. The occurrence of RFD surges adjacent to the right flank of the Tuscaloosa tornado during its intensification phase was suggested by Karstens et al. (2013) around the times the Chandler/Hughett's and Deelo's videos were taken and just before Rosolowski's video (Fig. 5). Thus, consistent with previous studies, frictional and/or baroclinic processes very likely contributed to the formation of HVs observed in the Tuscaloosa tornado.

An additional interesting aspect present in both trailing HVs is that they episodically exhibit smaller vortices wrapping around their outer edges. This phenomenon occurs twice in the first trailing HV. In the first situation, a thin, quasi-vertical condensation tube appears near the tail of the trailing HV and
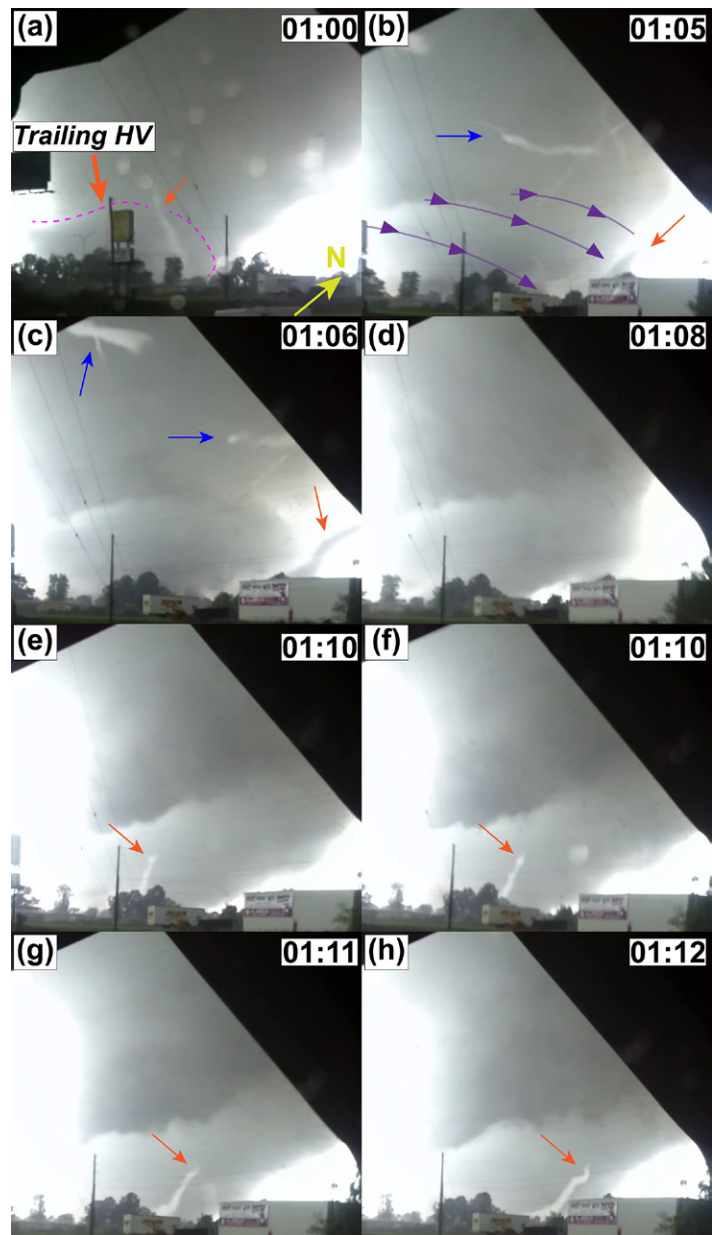

Fig. 6. (a)–(h) Image sequence showing the Tuscaloosa tornado as it passed north of the observer, exhibiting a large trailing HV. The magenta dashed line in (a) outlines the trailing HV due to the poor contrast with the tornado while purple streamlines in (b) roughly indicate the helical flow of the HV. The orange arrows denote the spiral vortices discussed in the text. Blue arrows show smaller-scale HVs advected by the tornado's outer flow. Times (MM:SS) are relative to the beginning of the video. Images provided through the courtesy of Tom Deelo.

moves along its periphery, as it rotates around the base of the tornado (orange arrows in Figs. 6a–c, 7b, and 7c; see the videos in the online supplemental material; https://doi.org/10.1175/BAMS-D-20-0251.2). The "head" of the vortex rotates under the trailing HV while its tail leans outward with height, such that their vertical vorticity component is clockwise. With time, the combined wind fields of the tornado and the trailing HV deform this vortex into a spiral[4] structure that is advected upward toward the cloud base

[4] This spiral vortex is referred to as a "coil-spring vortex" in Figs. 6a and 6b of Oliveira et al. (2019).

(Figs. 7d–g). A few seconds later, a similar (but smaller) vortex appears near the tail of the trailing HV and also moves along its outer edge and around the tornado (Figs. 6e–h and 7e–g). This second vortex develops a spiral structure in its tail in Figs. 6e–h and 7e–g. Multiple thin, wave-like vortices are also observed twisting around the tail of the second trailing HV (Figs. 8a,c,d). The systematic appearance of small vortices twisting around trailing HVs is, perhaps, a clue of the vortex dynamics involved in the formation of the latter. The formation mechanism of the trailing HV is discussed in the next section with the aid of the numerical simulation.

Simulated trailing HV

Three-dimensional structure and evolution.
The previous section provided evidence for the existence of trailing HVs based on videos of the Tuscaloosa tornado. Nevertheless,
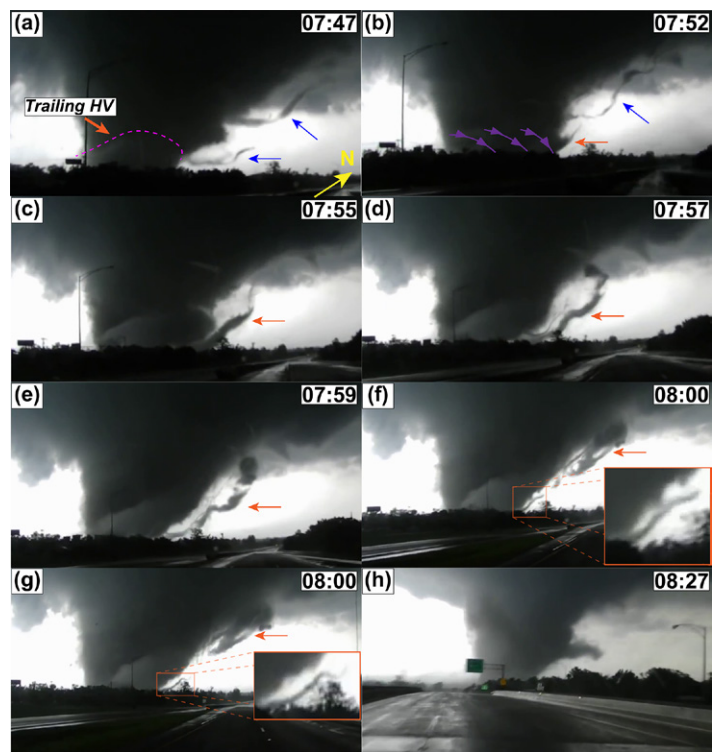

Fig. 7. (a)–(h) Image sequence showing the Tuscaloosa tornado as it passed north of the observers, exhibiting a large trailing HV. The magenta dashed line in (a) outlines the trailing HV due to the poor contrast with the tornado while purple streamlines in (b) roughly indicate the helical flow of the HV. The orange arrows denote the spiral vortices discussed in the text. The insets in (f) and (g) are zoomed-in views of the same spiral vortices. Blue arrows show smaller-scale HVs advected by the tornado's outer flow. Times (MM:SS) are relative to the beginning of the video. Images provided through the courtesy of Ryne Chandler and Nate Hughett.

analyses relying solely on visual observations are inherently limited to the HV segments revealed by the presence of cloud condensate, which does not necessarily show the full structure of trailing HVs. In this section, visualizations of a large simulated HV structure, which shares several characteristics with the observed trailing HVs, are employed to substantiate the visual observations and shed light on the 3D morphology of this type of HV.

Figure 9 shows volume-rendered plots of 3D vorticity magnitude throughout the life cycle of the simulated HV, which occurs through the fourth intensification and peak stages of the tornado (9,500–9,800 s; see also Figs. 3e and 4). The vorticity field is visualized because it is the most important indicator of the vortex tubes composing the trailing HV as well as other vortical structures in the flow.[5] At 9,500 s (Fig. 9a), the tornado is seen from the northeast as a northward-leaning tube, with its main axis denoted by the dashed red line. Several vortex tubes exist in the cold pool and around the tornado, but more prominently in the low levels of the rear-flank outflow south of the tornado. Some of these vortices are located adjacent to the ground, extending horizontally far north into the east side of the tornado, where they gently tilt upward (the main vortex axis is denoted by the dashed orange line). Between 9,550 and 9,600 s (Figs. 9b,c), other vortices originating in the rear-flank outflow

[5] The HVs are not revealed well when visualizing the cloud water field in our simulation; in fact, the condensation funnel of the tornado does not fully reach the ground in our simulation using the National Severe Storm Laboratory (NSSL) microphysics scheme (Mansell et al. 2010). A similar issue also occurs in the tornado-resolving simulation of Finley et al. (2018). The lack of condensation in the simulated vortices may be because that the pressure drop within the vortex tubes are not large enough due to the still relatively low resolution compared to the tube size; the simulated tubes are likely wider and weaker than observed tubes. The underlying physics of the HV should at least be qualitatively correct, however.
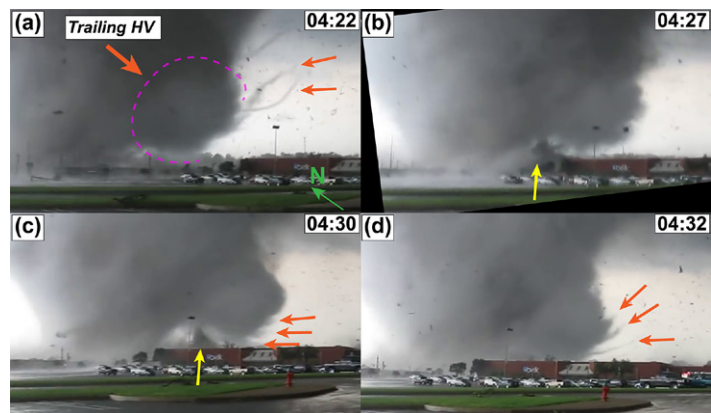
impinge on the incipient trailing HV, resulting in a larger, more complex structure. The position of the trailing HV relative to the tornado and the upward tilt near the tornado's forward sector are consistent with observed trailing HVs in Figs. 6 and 7, although its length (~1,000–2,000 m) and width (~150–300 m) are somewhat larger than the visually observed HVs (length < 1,000 m, width ~100–200 m); such difference may partially be due to that condensation only forms in the strongest section of the trailing HV in the vicinity of the tornado. Also similar to the real trailing HVs (Figs. 6–8), the rotation in the vortices constituting the simulated trailing HV is dominated by strong helical flow

Fig. 8. (a)–(d) Image sequence showing the Tuscaloosa tornado as it passed just north of the observer, exhibiting a large trailing HV, denoted by the large orange arrow and outlined by the dashed magenta line in (a). The small orange arrows denote the spiral vortices discussed in the text. Yellow arrows show damage to buildings at the interface of the tornado and the trailing HV. The frame shown in (b) was rotated counterclockwise by 7° to account for the unsteadiness of the footage. Times (MM:SS) are relative to the beginning of the video. Images provided through the courtesy of Jason Rosolowski.
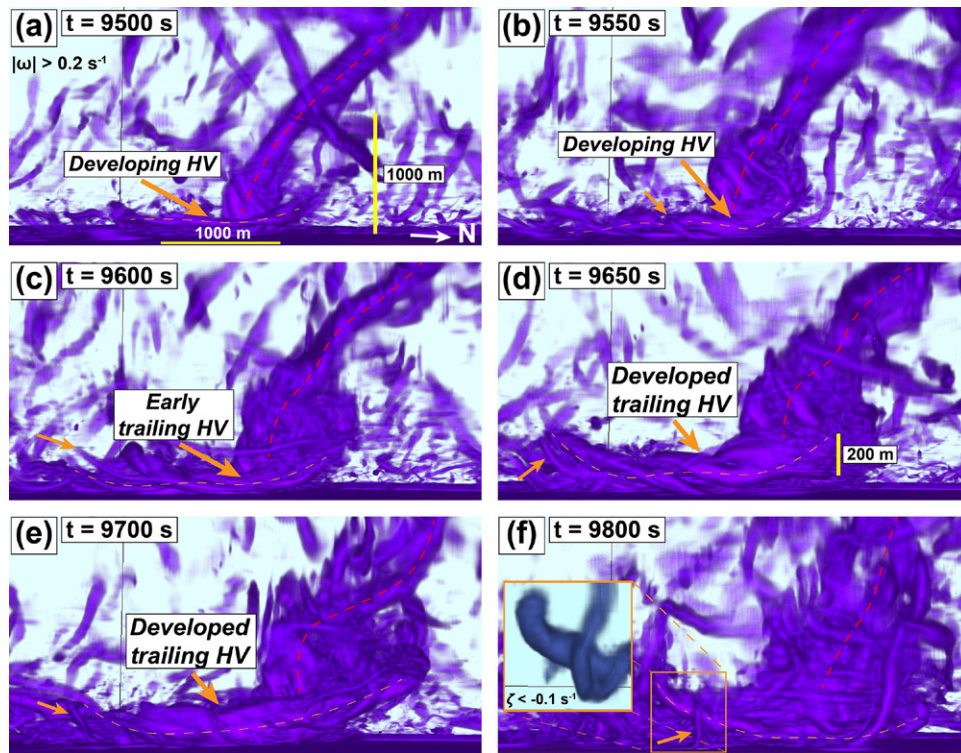
and associated vorticity vector directed from its tail into the tornado's forward sector (see the animation in the online supplemental material).

From 9,650 s to 9,700 s (Figs. 9d,e), the continuous interactions of smaller vortices with the trailing HV cause the HV structure to evolve from initially quasi-horizontal vortices into a large, complex entanglement of vortex tubes, extending further into the rear-flank of the storm, but preserving similar orientation relative to the tornado. The entangled vortex is composed of a spectrum of quasi-horizontal vortices, with the larger vortices contributing mostly to the structure of the trailing HV. As the tornado becomes completely wrapped in rain and weakens (Figs. 3e,f and 4), the trailing HV falls apart into a disorganized structure of intertwined vortices (Figs. 9f). The entangling process associated with the trailing HV structure resembles the entangling of quasi-parallel vortex tubes described in simulations of turbulent flows (e.g., Jiménez et al. 1993), which occurs as a result of the self-induced velocity fields of the individual vortices via the Biot–Savart law (Wu et al. 2007; Davidson 2015).

The entangled nature of trailing HVs is also associated with the development of the small spiral vortices observed in Figs. 6–8. From 9,550 to 9,800 s (Figs. 9b–h), smaller vortices (denoted by orange arrows) form near the tail of the trailing HV and move along it, until they rotate around the tornado, similar to the thin vortices in Figs. 6–8. Being smaller and weaker than the larger vortices composing the trailing HV, the smaller vortices are twisted by the bulk rotation of the trailing HV, causing their tail to lean outward and their "head" to move under the larger (parent) HV structure. This tilts the small, initially quasi-horizontal vortices containing mostly streamwise vorticity into a nearly vertical orientation dominated by anticyclonic vertical vorticity, distorting them into spiral structures (inset in Fig. 9f; also seen in Figs. 6c–h and 7f,g). These small vortices, when eventually absorbed into the trailing HV, head first, can, however, still contribute positively to cyclonic vertical vorticity when the leading part of the trailing HV is lifted off the ground.

Further insight into the structure of the simulated trailing HV and its association with nearby substorm-scale features is provided in the top view of the volume-rendered vorticity

Fig. 9. Volume-rendered plots of 3D vorticity magnitude ($|\omega|$), where $|\omega| > 0.2$ s^{-1} at (a) 9,500, (b) 9,550, (c) 9,600, (d) 9,650, (e) 9,700, and (f) 9,800 s. The orange dashed line indicates the approximate axis of the trailing HV structure. The red dashed line subjectively denotes the tornado axis. Large and small orange arrows indicate, respectively, the trailing HV and the downward-bending tails of the trailing HV similar to the observed small spiral vortices shown in Figs. 6–8. The anticyclonic character of the spiral vortices is highlighted in the inset in (f), where $\zeta < -0.1$ s^{-1} is shown in blue. The camera points to the southwest.

field (Fig. 10). At 9,500 s, the large HVs constituting the trailing HV are located to the east and southeast of the tornado, surrounded by smaller HVs. Near the surface, the large HVs are located immediately rearward of a rear-flank internal boundary or wind-shift line located to the southeast of the tornado near the surface (Fig. 11a). Farther east and aloft (Figs. 11b), the large HVs are located east of and along a similar internal boundary east of the surface boundary. These boundaries serve as a focus or convergence zone for accumulation of vortex tubes originated in the rear-flank outflow from the west. This is seen in the following 150 s (Figs. 10b–d), as more HVs continue to form in the rear-flank outflow and in the vicinity of the boundaries and progressively intertwine around the largest vortices, giving rise to the complex entangled structure that constitutes the trailing HV. The rear-flank internal boundaries also act as corridors of strong rear inflow toward the tornado as the westerly internal flow turns northward near and at the boundaries; as a result, the near-ground horizontal vorticity changes from predominantly crosswise in flows west of the boundaries to mostly streamwise in the direction of the turned flow due to the river-bend effect (Davies-Jones et al. 2001; Roberts et al. 2016) (Figs. 11b,c). As previously discussed, the crosswise horizontal vorticity is likely attributed to frictional torques and/or baroclinity along warm RFD surges (both mechanisms may act constructively along the warmer tongue west of $y = 46.7$ km in Fig. 11c and west of $y = 47$ km in Fig. 11d).

The internal boundary feature is also a favorable region for intensification of the trailing HV, as the HVs accumulate and are stretched in the along-boundary direction. This is evidenced by horizontal cross sections of horizontal streamwise vorticity and its stretching term shown in Figs. 11c–f. The trailing HV is located just to the west of the boundary-related
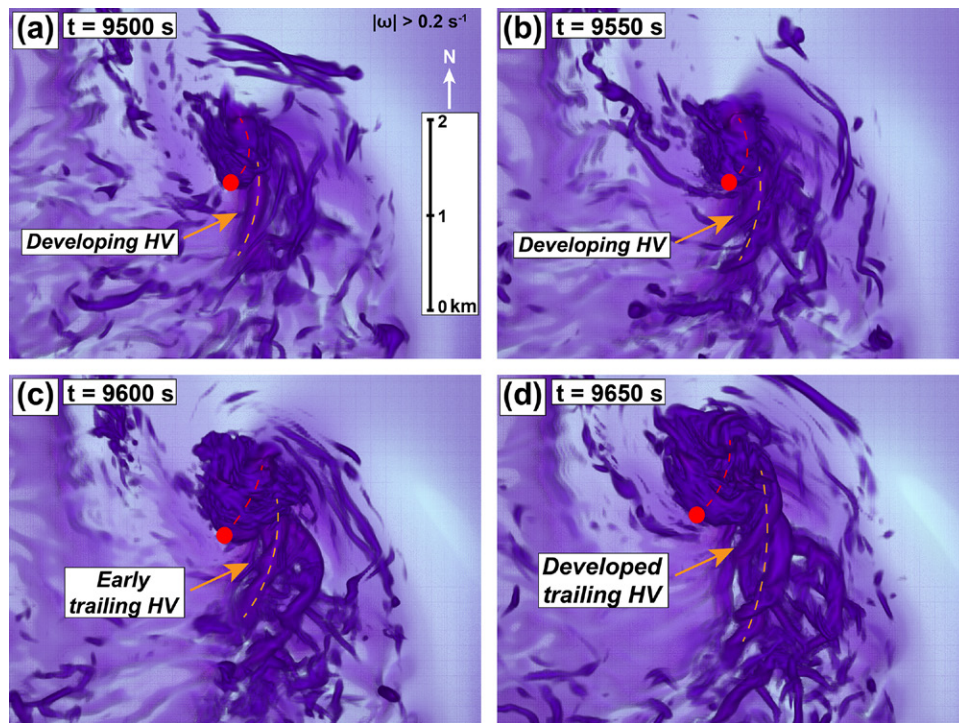
Fig. 10. Top view of volume-rendered 3D vorticity magnitude ($|\omega|$) where $|\omega| > 0.2$ s^{-1} at (a) 9,500, (b) 9,550, (c) 9,600, and (d) 9,650 s. The vorticity field is rendered only between the surface and 1 km AGL to avoid contamination by other intervening structures. The red dashed line subjectively denotes the tornado axis, with the red circle representing the base of the tornado; similarly, the orange dashed line denotes the main axis of the trailing HV structure. The camera is located at 5 km AGL.

wind shifts, where the flow turns leftward then rapidly accelerates toward the east sector of the tornado, resulting in corridors of intense streamwise vorticity (Figs. 11a,b) due to crosswise-to-streamwise exchange then stretching (Figs. 11e,f) (though some zones of vorticity compression exist where the flow slows down or changes direction abruptly). This relationship between the HV and the rear-flank internal boundaries substantiates the analysis based on the visual observations (Figs. 6–8) and the visualizations of vorticity (Fig. 9), which highlight the trailing HV as a strong helical vortex in the east-southeast sector of the tornado.

Near-surface wind field. A question raised in the introduction was, "Can tornado–HV interactions enhance damaging winds at the surface?" The observed damage at the interface between the tornado and the trailing HV in Figs. 8b and 8c suggest so. We now further address this question by inspecting the intensity of the near-surface horizontal and vertical velocity fields near the interface between the simulated tornado the trailing HV. Figure 12 show horizontal cross sections of ground-relative horizontal wind speed, vertical velocity, and streamwise horizontal vorticity at 30 and 225 m AGL on an area encompassing the tornado and the trailing HV at 9,610 s during the mature phase of the HV. These 30 and 225 m AGL levels are shown because they are located near the cores of two large HVs (Fig. 11) that compose the broader trailing HV structure shown in Figs. 9 and 10. As expected for a fast forward-moving tornado, ground-relative winds are stronger at its eastern periphery (Fig. 12a,b); this location also coincides with the north portion of the lower (and smaller) trailing HV west of the westernmost internal boundary (Figs. 12e,f). The area of strong horizontal winds is also collocated with a band of intense upward motion (Figs. 12c,d) in the eastern sector of the tornado. This is the area where the tornado draws in and stretches horizontal streamwise vorticity along the internal boundaries, as identified in Figs. 11, 12e, and 12f. In turn, the upper
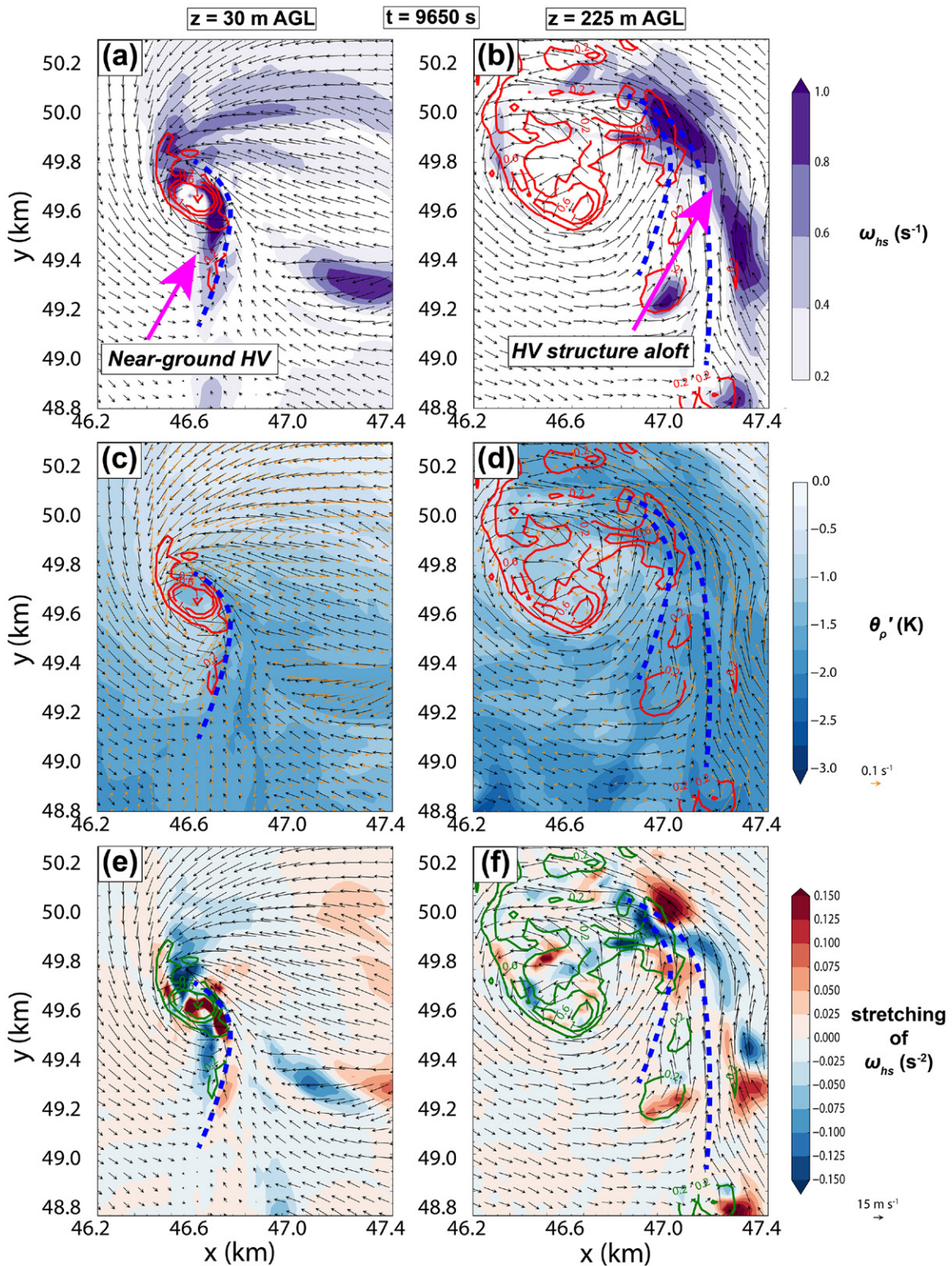
Fig. 11. (a),(b) Streamwise horizontal vorticity (shaded; s⁻¹), (c),(d) density potential temperature perturbation (θ_ρ'; shaded; K) and horizontal vorticity (orange vectors; s⁻¹), and (e),(f) stretching of horizontal streamwise vorticity (shaded; s⁻²). The red [green] contours in (a)–(d) [(e) and (f)] represent vertical vorticity in the tornado beginning at $\zeta = 0.2$ s⁻¹, plotted at 0.4-s⁻¹ intervals. Black vectors in all plots are storm-relative winds. The thick blue dashed line indicates the wind-shift line associated with rear-flank internal boundaries. The magenta arrows in (a) and (b) denote the HV. The fields in the left (right) column are plotted at 30 m (225 m) AGL. All fields are valid at 9,650 s.

HV (just east of the easternmost boundary) is much larger (Fig. 12f) and stronger (Figs. 12b and 12d) than the smaller one the west, with its wind field clearly discernible from the tornado itself. A closer look into the vertical structure of the HVs and their wind fields is presented through vertical cross sections at y = 49.5 km, shown in Fig. 13. The superposition of the HVs and the tornado wind fields induces rotor-type circulations containing extremely strong winds. The lower branch of the large HV contains ground-relative wind speeds > 50 m s^{-1} at the surface east of the tornado and > 90 m s^{-1} between 125 and 200 m AGL near its core (Fig. 13a). This vortex also produces strong updrafts > 10–20 m s^{-1} just above the surface (10–40 m AGL) (Fig. 13b) and similarly strong downdrafts. The rotor-type structure of the smaller HV is less discernible from the tornado's secondary circulation itself, though it is apparent as an area of the enhanced streamwise horizontal vorticity below 100 m AGL.

Hence, the analysis based on Figs. 12 and 13 suggests that trailing HVs are associated with both enhanced ground-relative horizontal and vertical winds at the right edges of tornadoes to some extent. This is especially true for the large HV in Figs. 12 and 13, which contains strong winds around its core that extend toward the surface. Unfortunately, however, such conclusions based on a single simulated event are, at most, circumstantial, since it is impossible to know exactly how the unsteady, highly asymmetric tornado would have evolved in the absence of the trailing HV. This is mostly the case for the smaller HV structure, as it overlaps with the tornado secondary circulation itself. More studies addressing the interactions of large HVs and tornadoes are necessary to understand how near-tornado wind fields are affected by the presence of HVs.

Discussion and conclusions

A combined analysis of videos of the 27 April 2011 Tuscaloosa EF4 tornado and 3D visualizations of an idealized supercell simulation at 30-m horizontal grid spacing for the same tornado case reveals a distinct type of HV structure termed "trailing HV." This type of vortex trails the tornado while attached to its right flank just above the surface, producing visually impressive helical motions consistent with vorticity generation via surface friction or baroclinity along warm RFD internal boundaries. Unlike some previously documented HVs, which are typically much smaller than the tornado and move along with its outer flow, trailing HVs are larger and strong enough to interact with the tornado and maintain a semisteady tornado-relative position before eventually being advected around the tornado. An intriguing aspect of trailing HVs is that they occasionally display smaller vortices wrapping around them. The tail of these vortices leans outward with height while the vortices move crosswise relative to the outer periphery of the trailing HV axis and rotate around the base of the tornado, such that their vertical component of vorticity is clockwise or anticyclonic. When reaching the forward sector of the tornado, they may evolve into spiral structures with the leading portion being advected upward into the tornado's upper flow and contribute cyclonic vorticity to tornado circulation. In the case of the small vortices discussed here though, vortex breakdown dynamics seems unlikely to explain their spiral structures, since they do not appear to be rooted at the ground as vertical vortices and may be later advected upward. Rather, it seems plausible to assume that, based on the tornado videos and simulation visualizations, the spiral structures result from the combined wind fields of the trailing HV and the tornado acting to deform the smaller vortices.

Visualizations of the simulated 3D vorticity magnitude field show that the trailing HV forms as an amalgamation of mainly streamwise HVs originating in the storm's near-surface rear-flank outflow (presumably produced mainly by frictional effects) west and south of the tornado. Internal convergence boundaries attached to the east-southeast flank of the tornado act as corridors where the HVs accumulate, realign (with the flow turning into the direction of the HV's rotation axis so that the horizontal velocity and vorticity vectors become aligned and
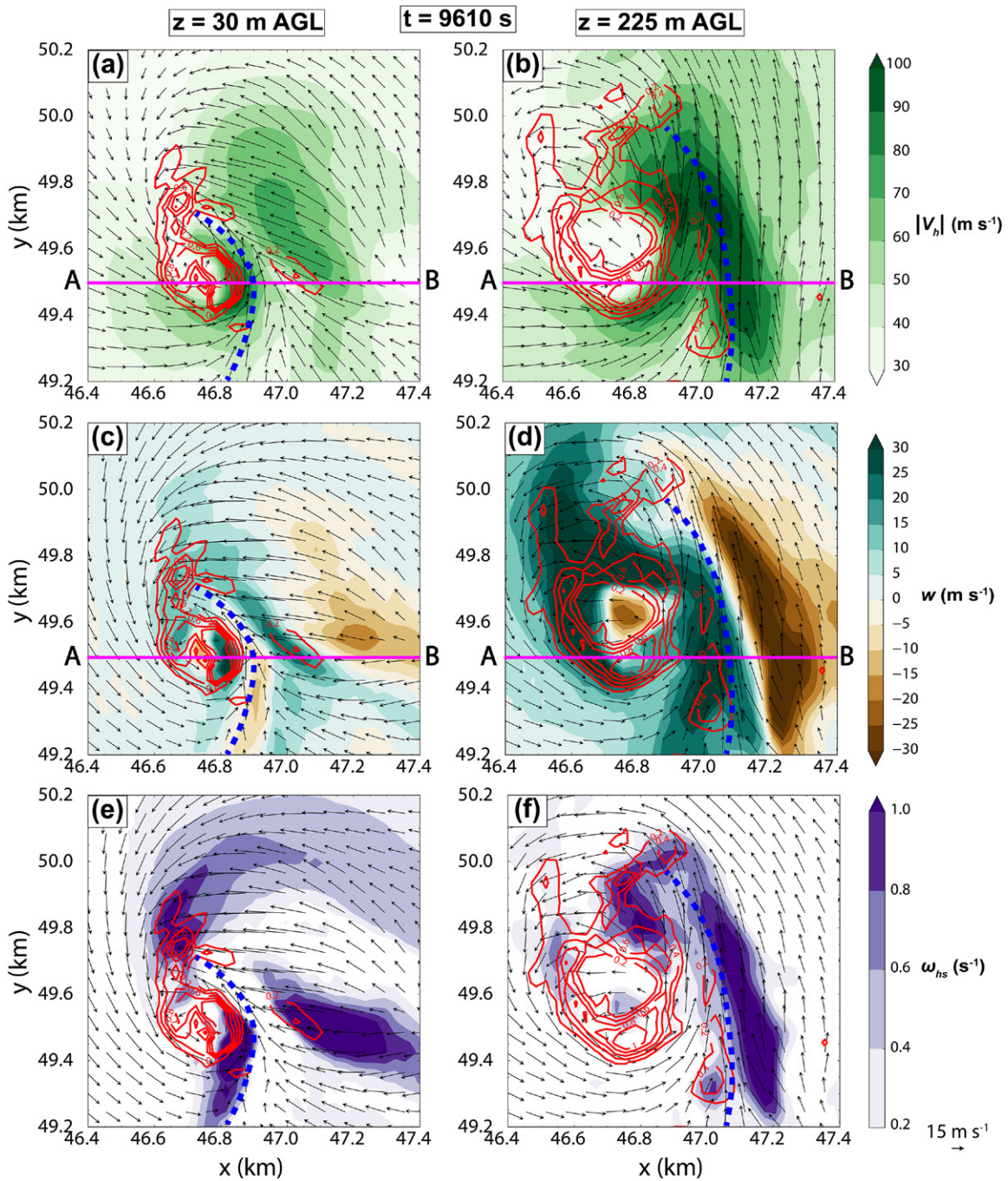
Fig. 12. Horizontal cross sections of (a),(b) ground-relative horizontal wind speed ($|V_h|$; shaded; m s^{-1}), (c),(d) vertical velocity (w; shaded; m s^{-1}), and (e),(f) streamwise horizontal vorticity (ω_{hs}; shaded; s^{-1}). Vectors are ground-relative winds in (a) and (b) and storm-relative in (c)–(f). The blue dashed line indicates the wind-shift line associated with a rear-flank internal boundary. The magenta AB line located along $y = 49.5$ km in (a)–(d) refers to the vertical cross sections shown in Fig. 13. In all panels, the red contours represent vertical vorticity in the tornado beginning at $\zeta = 0.2$ s^{-1}, plotted at 0.4-s^{-1} intervals. The fields in the left (right) column are plotted at 30 m (225 m) AGL. All fields are valid at 9,610 s.

the crosswise vorticity becomes streamwise), and are subsequently intensified via stretching of streamwise vorticity. The induced velocity field of neighboring quasi-parallel large HVs causes them to entangle in the vicinity of the boundaries and subsequently evolve into long intertwined vortices; this entangling process is the essence of the trailing HV structure. Furthermore, the vortex entangling process also explains the smaller, spiral vortices observed in the videos of the Tuscaloosa tornado. The small vortices, initially quasi horizontal, arise
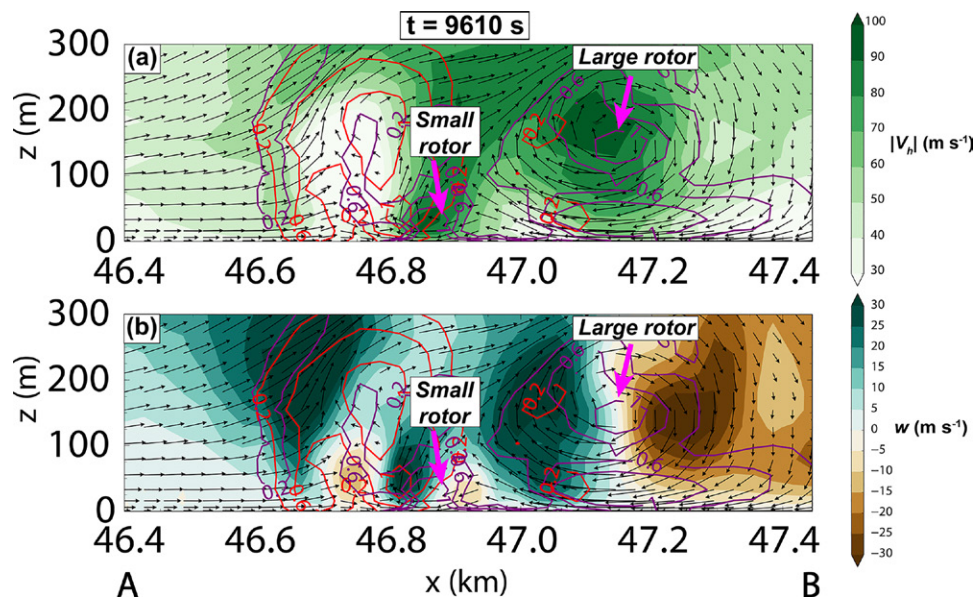
Fig. 13. Vertical cross sections of (a) $|V_h|$ and (b) w along the AB line shown in Fig. 12a–d. The purple contours denote streamwise horizontal vorticity beginning at $\omega_{hs} = 0.2$ s^{-1}, plotted at 0.4-s^{-1} intervals. In all panels, the red contours represent vertical vorticity in the tornado beginning at $\zeta = 0.2$ s^{-1}, plotted at 0.4-s^{-1} intervals. The magenta arrows denote the rotor-type circulations associated with the HVs. All fields valid at 9,610 s.

at the tail of the trailing HV and are twisted (i.e., tilted downward) by the trailing HV, such that their "heads" move underneath and along the trailing HV, while their tail becomes quasi vertical and rotates clockwise. Analogous entangling of quasi-parallel vortices is known to occur in low-Reynolds-number flow simulations, but has not been extensively studied in the context of supercell tornado research. The proposed formation mechanism of trailing HVs discussed above as swell as the HV relationship with the internal convergence boundary and smaller vortices are summarized in a conceptual model in Fig. 14.

One of the videos of the Tuscaloosa tornado (Rosolowski's video) shows damage to structures near the region where a trailing HV tangents the tornado. An analysis of the low-level winds during the mature stage of the simulated trailing HV shows that the combined wind fields of the tornado's outer updraft and the upward branch of the trailing HV resemble a rotor-type circulation that enhances horizontal winds very close to the surface, where significant damage may result. Other rotor-type circulations have been observed in simulated tornadic supercells (Schueth et al. 2021) and quasi-linear convective systems (Schenkman et al. 2012), and are associated with enhanced upward motion and horizontal vorticity. It is possible that large HVs in the vicinity of tornadoes such as the ones documented in this study account for some of the tornado damage, as long as they are present.

Finally, a few considerations regarding the visually observed and simulated trailing HVs must be made. First, the frequency of occurrence of trailing HVs is unknown among all tornadoes. These trailing HVs are larger-scale, more coherent versions of the weaker HVs typically seen near tornadoes, which is a result of their apparent association with rear-flank internal boundaries. It seems plausible to assume that similar structures occur in many strong/violent tornadoes, especially for HVs in the vicinity of rear-flank internal boundaries, but are not readily visible as condensation tubes (when the pressure drop inside is not large enough, at least away from the tornado). The ever-increasing availability of close-range mobile Doppler radar observations as well as more visual recordings of tornadoes can help better detect and document this phenomenon. Second, surface friction was suggested as a key vorticity generation mechanism for trailing HVs. This is an example of why neglecting surface drag in tornado simulations, as done in many studies prior to the past decade, may limit their
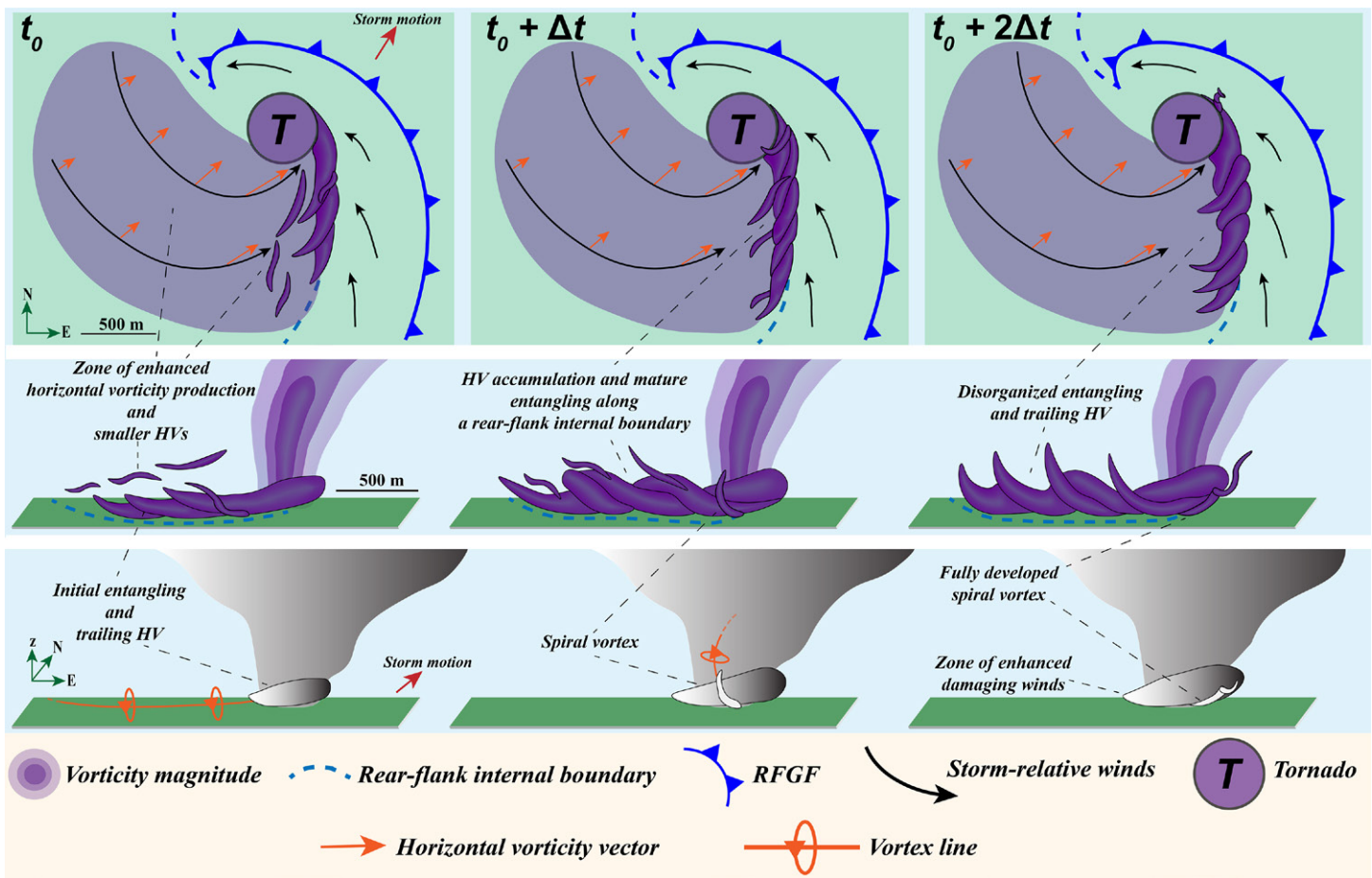
Fig. 14. Conceptual model for the evolution of the trailing HV and spiraling vortices as related to surrounding storm-scale features. (top) Top views of the 3D vorticity magnitude field. (middle) The 3D vorticity magnitude field viewed from the northeast. (bottom) Cloud field consistent with the visual observations viewed from the southeast. In all panels, time advances from the left to the right. All relevant symbols are defined in the bottom section of the figure. At t_0, predominantly crosswise horizontal vorticity, which is produced in the rear-flank outflow, evolves into coherent HVs that align and accumulate in the vicinity of an internal boundary east-southeast of the tornado. As large and small HVs interact in that zone, their self-induced wind fields initiate an entangling process. By $t_0 + \Delta t$, the HVs have fully intertwined and grown into a complex vortex entanglement, visually observed as a large helical HV. As the entangling continues, some smaller HVs as well as the tails of the larger HVs may bend downward, producing small spiraling anticyclonic vortices in the outer edge of the HV. By $t_0 + 2\Delta t$, the entangling begins to disorganize, as seen by the increasingly distortion larger vortices composing the trailing HVs. Spiral vortices continue to occur during this stage.

realism in a meaningful way. Nevertheless, it is known that the use of semislip lower boundary conditions in severe storm simulations can be problematic, resulting in overestimation of near-ground vertical shear in the storm's inflow in the absence of sufficient turbulence (Markowski and Bryan 2016) and underestimation in the outflow due to violations of the Monin–Obukhov similarity assumptions (Markowski et al. 2019). The parameterization of subgrid-scale turbulence near the ground surface or a rigid wall also needs improvement (Chow et al. 2005). However, the reasonable match between the visual observations of the trailing HVs and their simulated counterpart suggest that these issues do not hamper the qualitative interpretation of the results presented in this study. Last, the results also underscore the importance of studying interactions between tornadoes and the turbulent outflow of their parent storm (Takahashi et al. 2005). Further investigation of these processes can lead to a broader understanding of the spectrum of behaviors and structures that tornadoes display in nature. Detailed quantitative analyses of the vorticity sources of HVs and other related processes are underway and will be reported elsewhere.

References

Bai, L., and Coauthors, 2017: An integrated damage, visual, and radar analysis of the 2015 Foshan, Guangdong, EF3 tornado in China produced by the landfalling Typhoon Mujigae (2015). *Bull. Amer. Meteor. Soc.*, **98**, 2619–2640, https://doi.org/10.1175/BAMS-D-16-0015.1.

Chow, F. K., R. L. Street, M. Xue, and J. H. Ferziger, 2005: Explicit filtering and reconstruction turbulence modeling for large-eddy simulation of neutral boundary layer flow. *J. Atmos. Sci.*, **62**, 2058–2077, https://doi.org/10.1175/JAS3456.1.

Coffer, B. E., and M. D. Parker, 2017: Simulated supercells in nontornadic and tornadic VORTEX2 environments. *Mon. Wea. Rev.*, **145**, 149–180, https://doi.org/10.1175/MWR-D-16-0226.1.

——, and ——, 2018: Is there a "tipping point" between simulated nontornadic and tornadic supercells in VORTEX2 environments? *Mon. Wea. Rev.*, **146**, 2667–2693, https://doi.org/10.1175/MWR-D-18-0050.1.

——, ——, J. M. L. Dahl, L. J. Wicker, and A. J. Clark, 2017: Volatility of tornadogenesis: An ensemble of simulated nontornadic and tornadic supercells in VORTEX2 environments. *Mon. Wea. Rev.*, **145**, 4605–4625, https://doi.org/10.1175/MWR-D-17-0152.1.

——, ——, R. L. Thompson, B. T. Smith, and R. E. Jewell, 2019: Using near-ground storm relative helicity in supercell tornado forecasting. *Wea. Forecasting*, **34**, 1417–1435, https://doi.org/10.1175/WAF-D-19-0115.1.

Dahl, J. M. L., 2021: Centrifugal waves in tornado-like vortices: Kelvin's solutions and their applications to multiple-vortex development and vortex breakdown. *Mon. Wea. Rev.*, **149**, 3173–3216, https://doi.org/10.1175/MWR-D-20-0426.1.

Davidson, P. A., 2015: *Turbulence: An Introduction for Scientists and Engineers.* Oxford University Press, 630 pp.

Davies-Jones, R., 2021: Invented forces in supercell models. *J. Atmos. Sci.*, **78**, 2927–2939, https://doi.org/10.1175/JAS-D-21-0082.1.

——, R. J. Trapp, and H. B. Bluestein, 2001: Tornadoes and tornadic storms. *Severe Convective Storms*, *Meteor. Monogr.*, No. 50, Amer. Meteor. Soc., 167–222, https://doi.org/10.1175/0065-9401-28.50.167.

Dawson, D. T., M. Xue, J. A. Milbrandt, and A. Shapiro, 2015: Sensitivity of real-data simulations of the 3 May 1999 Oklahoma City tornadic supercell and associated tornadoes to multimoment microphysics. Part I: Storm- and tornado-scale numerical forecasts. *Mon. Wea. Rev.*, **143**, 2241–2265, https://doi.org/10.1175/MWR-D-14-00279.1.

——, B. Roberts, and M. Xue, 2019: A method to control the environmental wind profile in idealized simulations of deep convection with surface friction. *Mon. Wea. Rev.*, **147**, 3935–3954, https://doi.org/10.1175/MWR-D-18-0462.1.

Edwards, R., J. G. LaDue, J. T. Ferree, K. Scharfenberg, C. Maier, and W. L. Coulbourne, 2013: Tornado intensity estimation: Past, present, and future. *Bull. Amer. Meteor. Soc.*, **94**, 641–653, https://doi.org/10.1175/BAMS-D-11-00006.1.

Fiedler, B., 2009: Suction vortices and spiral breakdown in numerical simulations of tornado-like vortices. *Atmos. Sci. Lett.*, **10**, 109–114, https://doi.org/10.1002/asl.217.

Finley, C. A., L. Orf, B. D. Lee, and R. B. Wilhelmson, 2018: High-resolution simulation of a violent tornado in the 27 April 2011 outbreak environment. *29th Conf. on Severe Local Storms*, Stowe, VT, Amer. Meteor. Soc., 10B.5, https://ams.confex.com/ams/29SLS/webprogram/Paper348812.html.

Fischer, J., and J. M. L. Dahl, 2022: Transition of near-ground vorticity dynamics during tornadogenesis. *J. Atmos. Sci.*, **79**, 467–483, https://doi.org/10.1175/JAS-D-21-0181.1.

Flournoy, M. D., M. C. Coniglio, E. N. Rasmussen, J. C. Furtado, and B. E. Coffer, 2020: Modes of storm-scale variability and tornado potential in VORTEX2 near- and far-field tornadic environments. *Mon. Wea. Rev.*, **148**, 4185–4207, https://doi.org/10.1175/MWR-D-20-0147.1.

Goldacker, N. A., and M. D. Parker, 2021: Low-level updraft intensification in response to environmental wind profiles. *J. Atmos. Sci.*, **78**, 2763–2781, https://doi.org/10.1175/JAS-D-20-0354.1.

Grasso, L. D., and W. R. Cotton, 1995: Numerical simulation of a tornado vortex. *J. Atmos. Sci.*, **52**, 1192–1203, https://doi.org/10.1175/1520-0469(1995)052<1192:NSOATV>2.0.CO;2.

Houser, J. L., H. B. Bluestein, and J. C. Snyder, 2016: A finescale radar examination of the tornadic debris signature and weak-echo reflectivity band associated with a large, violent tornado. *Mon. Wea. Rev.*, **144**, 4101–4130, https://doi.org/10.1175/MWR-D-15-0408.1.

Jiménez, J., A. A. Wray, P. G. Saffman, and R. S. Rogallo, 1993: The structure of intense vorticity in isotropic turbulence. *J. Fluid Mech.*, **255**, 65–90, https://doi.org/10.1017/S0022112093002393.

Karstens, C. D., W. A. Gallus, B. D. Lee, and C. A. Finley, 2013: Analysis of tornado-induced tree fall using aerial photography from the Joplin, Missouri, and Tuscaloosa–Birmingham, Alabama, tornadoes of 2011. *J. Appl. Meteor. Climatol.*, **52**, 1049–1068, https://doi.org/10.1175/JAMC-D-12-0206.1.

Klemp, J. B., and R. B. Wilhelmson, 1978: The simulation of three-dimensional convective storm dynamics. *J. Atmos. Sci.*, **35**, 1070–1096, https://doi.org/10.1175/1520-0469(1978)035<1070:TSOTDC>2.0.CO;2.

——, and R. Rotunno, 1983: A study of the tornadic region within a supercell thunderstorm. *J. Atmos. Sci.*, **40**, 359–377, https://doi.org/10.1175/1520-0469(1983)040<0359:ASOTTR>2.0.CO;2.

Knupp, K. R., and Coauthors, 2014: Meteorological overview of the devastating 27 April 2011 tornado outbreak. *Bull. Amer. Meteor. Soc.*, **95**, 1041–1062, https://doi.org/10.1175/BAMS-D-11-00229.1.

Lemon, L. R., and C. A. Doswell III, 1979: Severe thunderstorm evolution and mesocyclone structure as related to tornadogenesis. *Mon. Wea. Rev.*, **107**, 1184–1197, https://doi.org/10.1175/1520-0493(1979)107<1184:STEAMS>2.0.CO;2.

Li, S., S. Jaroszynski, S. Pearse, L. Orf, and J. Clyne, 2019: VAPOR: A visualization package tailored to analyze simulation data in Earth system science. *Atmosphere*, **10**, 488, https://doi.org/10.3390/atmos10090488.

Mansell, E. R., C. L. Ziegler, and E. C. Bruning, 2010: Simulated electrification of a small thunderstorm with two-moment bulk microphysics. *J. Atmos. Sci.*, **67**, 171–194, https://doi.org/10.1175/2009JAS2965.1.

Markowski, P. M., 2016: An idealized numerical simulation investigation of the effects of surface drag on the development of near-surface vertical vorticity in supercell thunderstorms. *J. Atmos. Sci.*, **73**, 4349–4385, https://doi.org/10.1175/JAS-D-16-0150.1.

——, and Y. P. Richardson, 2014: The influence of environmental low-level shear and cold pools on tornadogenesis: Insights from idealized simulations. *J. Atmos. Sci.*, **71**, 243–275, https://doi.org/10.1175/JAS-D-13-0159.1.

——, and G. H. Bryan, 2016: LES of laminar flow in the PBL: A potential problem for convective storm simulations. *Mon. Wea. Rev.*, **144**, 1841–1850, https://doi.org/10.1175/MWR-D-15-0439.1.

——, N. T. Lis, D. D. Turner, T. R. Lee, and M. S. Buban, 2019: Observations of near-surface vertical wind profiles and vertical momentum fluxes from VORTEX-SE 2017: Comparisons to Monin–Obukhov similarity theory. *Mon. Wea. Rev.*, **147**, 3811–3824, https://doi.org/10.1175/MWR-D-19-0091.1.

Marquis, J. N., Y. P. Richardson, P. M. Markowski, D. Dowell, and J. Wurman, 2012: Tornado maintenance investigated with high-resolution dual-Doppler and EnKF analysis. *Mon. Wea. Rev.*, **140**, 3–27, https://doi.org/10.1175/MWR-D-11-00025.1.

Moeng, C.-H., and J. C. Wyngaard, 1988: Spectral analysis of large-eddy simulations of the convective boundary layer. *J. Atmos. Sci.*, **45**, 3573–3587, https://doi.org/10.1175/1520-0469(1988)045<3573:SAOLES>2.0.CO;2.

Noda, A. T., and H. Niino, 2010: A numerical investigation of a supercell tornado: Genesis and vorticity budget. *J. Meteor. Soc. Japan*, **88**, 135–159, https://doi.org/10.2151/jmsj.2010-203.

Oliveira, M. I., M. Xue, B. Roberts, and L. J. Wicker, 2019: Horizontal vortex tubes near tornadoes: Three-dimensional structure and dynamics. *Atmosphere*, **10**, 716, https://doi.org/10.3390/atmos10110716.

Orf, L., 2019: A violently tornadic supercell thunderstorm simulation spanning a quarter-trillion grid volumes: Computational challenges, I/O framework, and visualizations of tornadogenesis. *Atmosphere*, **10**, 578, https://doi.org/10.3390/atmos10100578.

——, R. Wilhelmson, B. Lee, C. Finley, and A. Houston, 2017: Evolution of a long-track violent tornado within a simulated supercell. *Bull. Amer. Meteor. Soc.*, **98**, 45–68, https://doi.org/10.1175/BAMS-D-15-00073.1.

Rasmussen, E., 2003: Refined supercell and tornado forecast parameters. *Wea. Forecasting*, **18**, 530–535, https://doi.org/10.1175/1520-0434(2003)18<530:RSATFP>2.0.CO;2.

Roberts, B., and M. Xue, 2017: The role of surface drag in mesocyclone intensification leading to tornadogenesis within an idealized supercell simulation. *J. Atmos. Sci.*, **74**, 3055–3077, https://doi.org/10.1175/JAS-D-16-0364.1.

——, ——, A. D. Schenkman, and D. T. Dawson, 2016: The role of surface drag in tornadogenesis within an idealized supercell simulation. *J. Atmos. Sci.*, **73**, 3371–3395, https://doi.org/10.1175/JAS-D-15-0332.1.

——, ——, and D. T. Dawson, 2020: The effect of surface drag strength on mesocyclone intensification and tornadogenesis in idealized supercell simulations. *J. Atmos. Sci.*, **77**, 1699–1721, https://doi.org/10.1175/JAS-D-19-0109.1.

Rotunno, R., and J. Klemp, 1985: On the rotation and propagation of simulated supercell thunderstorms. *J. Atmos. Sci.*, **42**, 271–292, https://doi.org/10.1175/1520-0469(1985)042<0271:OTRAPO>2.0.CO;2.

Schenkman, A. D., M. Xue, and A. Shapiro, 2012: Tornadogenesis in a simulated mesovortex within a mesoscale convective system. *J. Atmos. Sci.*, **69**, 3372–3390, https://doi.org/10.1175/JAS-D-12-038.1.

——, ——, and M. Hu, 2014: Tornadogenesis in a high-resolution simulation of the 8 May 2003 Oklahoma City supercell. *J. Atmos. Sci.*, **71**, 130–154, https://doi.org/10.1175/JAS-D-13-073.1.

——, ——, and D. T. Dawson II, 2016: The cause of internal outflow surges in a high-resolution simulation of the 8 May 2003 Oklahoma City tornadic supercell. *J. Atmos. Sci.*, **73**, 353–370, https://doi.org/10.1175/JAS-D-15-0112.1.

Schueth, A., C. Weiss, and J. M. L. Dahl, 2021: Comparing observations and simulations of the streamwise vorticity current and the forward-flank convergence boundary in a supercell storm. *Mon. Wea. Rev.*, **149**, 1651–1671, https://doi.org/10.1175/MWR-D-20-0251.1.

Skinner, P. S., C. C. Weiss, J. L. Schroeder, L. J. Wicker, and M. I. Biggerstaff, 2011: Observations of the surface boundary structure within the 23 May 2007 Perryton, Texas, supercell. *Mon. Wea. Rev.*, **139**, 3730–3749, https://doi.org/10.1175/MWR-D-10-05078.1.

Snook, N., and M. Xue, 2008: Effects of microphysical drop size distribution on tornadogenesis in supercell thunderstorms. *Geophys. Res. Lett.*, **35**, L24803, https://doi.org/10.1029/2008GL035866.

——, ——, and Y. Jung, 2019: Tornado-resolving ensemble and probabilistic predictions of the 20 May 2013 Newcastle–Moore EF5 tornado. *Mon. Wea. Rev.*, **147**, 1215–1235, https://doi.org/10.1175/MWR-D-18-0236.1.

Takahashi, N., H. Ishii, and T. Miyazaki, 2005: The influence of turbulence on a columnar vortex. *Phys. Fluids*, **17**, 035105, https://doi.org/10.1063/1.1858532.

Tao, T., and T. Tamura, 2020: Numerical study of the 6 May 2012 Tsukuba supercell tornado: Vorticity sources responsible for tornadogenesis. *Mon. Wea. Rev.*, **148**, 1205–1228, https://doi.org/10.1175/MWR-D-19-0095.1.

Taszarek, M., J. T. Allen, T. Púčik, K. A. Hoogewind, and H. E. Brooks, 2020: Severe convective storms across Europe and the United States. Part II: ERA5 environments associated with lightning, large hail, severe wind, and tornadoes. *J. Climate*, **33**, 10263–10286, https://doi.org/10.1175/JCLI-D-20-0346.1.

Wicker, L. J., and R. B. Wilhelmson, 1995: Simulation and analysis of tornado development and decay within a three-dimensional supercell thunderstorm. *J. Atmos. Sci.*, **52**, 2675–2703, https://doi.org/10.1175/1520-0469(1995)052<2675:SAAOTD>2.0.CO;2.

Wu, J.-Z., H.-Y. Ma, and M.-D. Zhou, 2007: *Vorticity and Vortex Dynamics.* Springer Science and Business Media, 776 pp.

Wurman, J., and K. Kosiba, 2013: Finescale radar observations of tornado and mesocyclone structures. *Wea. Forecasting*, **28**, 1157–1174, https://doi.org/10.1175/WAF-D-12-00127.1.

Xue, M., K. K. Droegemeier, and V. Wong, 2000: The Advanced Regional Prediction System (ARPS)—A multi-scale nonhydrostatic atmospheric simulation and prediction model. Part I: Model dynamics and verification. *Meteor. Atmos. Phys.*, **75**, 161–193, https://doi.org/10.1007/s007030070003.

——, and Coauthors, 2001: The Advanced Regional Prediction System (ARPS)—A multi-scale nonhydrostatic atmospheric simulation and prediction model. Part II: Model physics and applications. *Meteor. Atmos. Phys.*, **76**, 143–165, https://doi.org/10.1007/s007030170027.

——, D.-H. Wang, J.-D. Gao, K. Brewster, and K. K. Droegemeier, 2003: The Advanced Regional Prediction System (ARPS), storm-scale numerical weather prediction and data assimilation. *Meteor. Atmos. Phys.*, **82**, 139–170, https://doi.org/10.1007/s00703-001-0595-6.

——, M. Hu, and A. D. Schenkman, 2014: Numerical prediction of the 8 May 2003 Oklahoma City tornadic supercell and embedded tornado using ARPS with the assimilation of WSR-88D data. *Wea. Forecasting*, **29**, 39–62, https://doi.org/10.1175/WAF-D-13-00029.1.

Yao, D., Z. Meng, and M. Xue, 2019: Genesis, maintenance and demise of a simulated tornado and the evolution of its preceding descending reflectivity core (DRC). *Atmosphere*, **10**, 236, https://doi.org/10.3390/atmos10050236.

Yokota, S., H. Niino, H. Seko, M. Kunii, and H. Yamauchi, 2018: Important factors for tornadogenesis as revealed by high-resolution ensemble forecasts of the Tsukuba supercell tornado of 6 May 2012 in Japan. *Mon. Wea. Rev.*, **146**, 1109–1132, https://doi.org/10.1175/MWR-D-17-0254.1.

Yussouf, N., D. C. Dowell, L. J. Wicker, K. H. Knopfmeier, and D. M. Wheatley, 2015: Storm-scale data assimilation and ensemble forecasts for the 27 April 2011 severe weather outbreak in Alabama. *Mon. Wea. Rev.*, **143**, 3044–3066, https://doi.org/10.1175/MWR-D-14-00268.1.